Microseismicity in the Krýsuvík Geothermal Field, SW Iceland, from May to October 2009

Sigríður Kristjánsdóttir

MICROSEISMICITY IN THE KRÝSUVÍK GEOTHERMAL FIELD, SW ICELAND, FROM MAY TO OCTOBER 2009

Sigríður Kristjánsdóttir

60 ECTS thesis submitted in partial fulfillment of a
Magister Scientiarum degree in Geophysics

Advisors
Kristján Ágústsson
Ólafur G. Flóvenz

Faculty Representative
Sigrún Hreinsdóttir

Faculty of Earth Sciences
School of Engineering and Natural Sciences
University of Iceland
Reykjavik, May 2013

Microseismicity in the Krýsuvík Geothermal Field, SW Iceland, from May to October 2009
Microseismicity in the Krýsuvík Geothermal Field
60 ECTS thesis submitted in partial fulfillment of a M.Sc. degree in Geophysics

I hereby declare that this thesis is written by me and is based on my own research. It has not before been submitted in part or in whole for the purpose of obtaining a higher degree.

_____

Sigríður Kristjánsdóttir

Abstract

Krýsuvík is a geothermal area located on the Reykjanes Peninsula in southwest Iceland. The Reykjanes Peninsula is an oblique plate spreading boundary under heavy influence of a mantle plume located beneath southeast Iceland. Intense seismic swarms occured in the area during alternating periods of uplift and subsidence in 2009 and 2011. A dense seismic network located in the area from May till October 2009 together with the regional seismic network of the Icelandic Meteorological Office recorded over ten thousand earthquakes. The activity was characterized by short, intense swarms in between longer, quieter periods. A detailed analysis was performed on the focal mechanisms of 1,063 events, including a stress tensor inversion for several swarms in the Krýsuvík and Fagradalsfjall areas. Interestingly, earthquakes of different faulting types characterize individual swarms, with normal, reverse, and strike-slip events taking place in the same swarms. Stress tensor inversion reveals a NW-SE trending minimum horizontal stress, in good agreement with previous studies in the area. No direct indication of magmatic involvement during the deformation sequence is observed.

Útdráttur

Á Krýsuvíkursvæðinu hefur bæði landris og landsig átt sér stað undanförnum árum. Tvær lotur þar sem landsig hefur fylgt landrisi hafa komið fram á árunum 2009-2012. Í bæði skiptin hefur orðið vart aukinnar skjálftavirkni á svæðinu í kjölfarið. Í maí 2009, á þeim tíma þegar landris var í gangi, var sett upp net 32 jarðskjálftamæla á Krýsuvíkursvæðinu. Mælingar stóðu yfir til október 2009. Auk þess fengust gögn úr mælum SIL-kerfis Veðurstofu Íslands. Í heildina voru skráðir yfir tíu þúsund jarðskjálftar. Virknin einkenndist af stuttum, áköfum hrinum inn á milli lengri, rólegri tímabila. Brotlausnir um eitt þúsund skjálfta voru rannsakaðar. Meðal annars var spennusviðið reiknað út frá brotlausnum nokkurra hrina á Krýsuvíkur- og Fagradalssvæðinu. Það vekur athygli að brotlausnir innan hverrar hrinu eru mjög breytilegar. Þannig finnast samgengis-, sniðgengis- og siggengisskjálftar í sömu hrinum. Útreikningar á spennusviðinu leiða í ljós að í flestum tilfellum stefnir minnsta lárétta spennan NV-SA. Þetta er í samræmi við niðurstöður annarra rannsókna á svæðinu. Ekkert bendir til þess að jarðskjálftarnir tengist kvikuumbrotum undir Krýsuvíkursvæðinu.

x

Acknowledgments

Last but not least, I am forever grateful for the effort of my family. My mom and dad are always available for advise and support. My inlaws are always prepared to lend a hand. My sister has been my go-to person when things are going both well and bad. My two beautiful daughters are a constant source of inspiration and amusement. I certainly couldn't have done this without my husband, who encouraged me when challenges arose and celebrated with me on joyous occations. Takk Stulli.

0

Contents

Contents

List of Figures

List of Tables

LIST OF TABLES

1 Theory

1.1 Source characteristics

1.1.1 Focal mechanism solutions

Focal mechanisms are used to describe the spatial characteristics of earthquakes, i.e. the direction of slip and the orientation of the fault. The mechanisms are often visually represented by so called beach balls. The beach balls are constructed from the radiation pattern of first P-wave arrivals. The P-waves are assumed to originate from a common source point. Their position on an imagined sphere around the source, called the focal sphere, is determined by two parameters: The azimuth from the source, ϕ_s, and the take-off angle, i_h. Depending on the orientation of the fault and slip, compressional and dilatational P-waves should systematically appear on different quadrants of the sphere. By marking compressional and dilatational P-waves differently on stereographic projection of the focal sphere a pattern should emerge (see Fig. 1.1). We should be able to split up this pattern with two lines signifying orthogonal planes which divide the focal sphere into quadrants. One of those planes is the fault plane of the earthquake. Due to an ambiguity inheritied in double-couple force system used to emulate the seismic soure other methods must be

used to confirm which is the correct fault plane. An example of a focal mechanism solution for an event in Krýsuvík recorded during a period of uplift in the area is shown in Fig. 1.2. The seismicity recorded during the uplift is the subject of the accompanying paper.
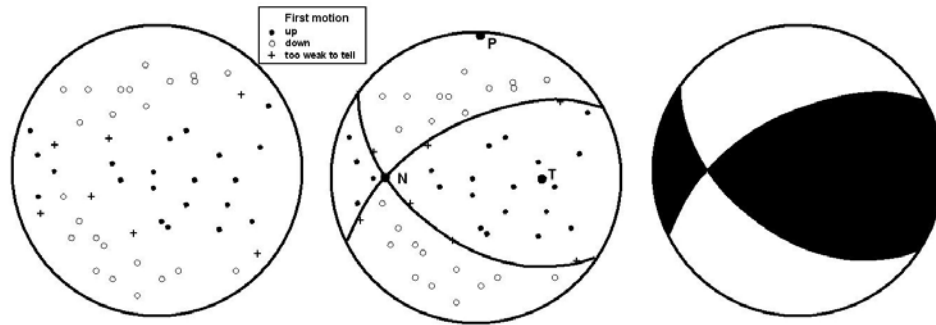
Figure 1.1: Lower-hemisphere stereographic projections of the focal sphere. Left: First P-wave arrivals marked as compressional (filled circle), dilatational (open circle), or ambigious (plus). Middle: Orthogonal planes drawn as intersecting lines splitting the focal sphere into quadrants. P marks the pressure axis, T marks the tensional axis and N lies on the intersection of the two planes, orthogonal to both P and T. Right: Beachball plot with quadrants colored according to P-wave motion, black=compressional and uncolored=dilatational.

On seimograms the P-wave presents itself as either going up or down, where up signals compressional motion and down dilatational motion. However, we must bear in mind that the stress condition in the compressional quadrant is dilatational at the source prior to the earthquake and vica versa the stress condition in the dilatational quadrant is compressional at the source. Therefore, a pressure axis (P) is defined in the dilatational quadrant and a tensional axis (T) in the compressional quadrant. These axes are orthogonal to each other and oriented 45° from the nodal planes. A third axis, the B-axis (N in Fig. 1.1), lies on the intersection of the two planes and is orthogonal to both the P and T axes. If we imagine that we cut the top of the focal sphere and look inside the bowl from above, we see the lower hemisphere projection of the focal mechanism. Compressional sections are traditionally colored

Mon Sep 5 12:51:06 2011

fin.prt

20 90726 4:27 36.26
63-53.39 22- 5.02
DEPTH = 2.15 KM
MAG = 0.89

RMS = 0.10 S
DMIN = 3 KM
AZM GAP = 180
FM = 10

ERH = 0.3 KM
ERZ = 0.2 KM
MISFIT = 0.00 (+.05)
STDR = 0.49

STRIKE UNCERTAINTY = 10
DIP UNCERTAINTY = 8
RAKE UNCERTAINTY = 10
% MACHINE PICKS = 0

P

T

135,45,120

276,52,63

UP DWN
O O DILATATION
+ + COMPRESSION
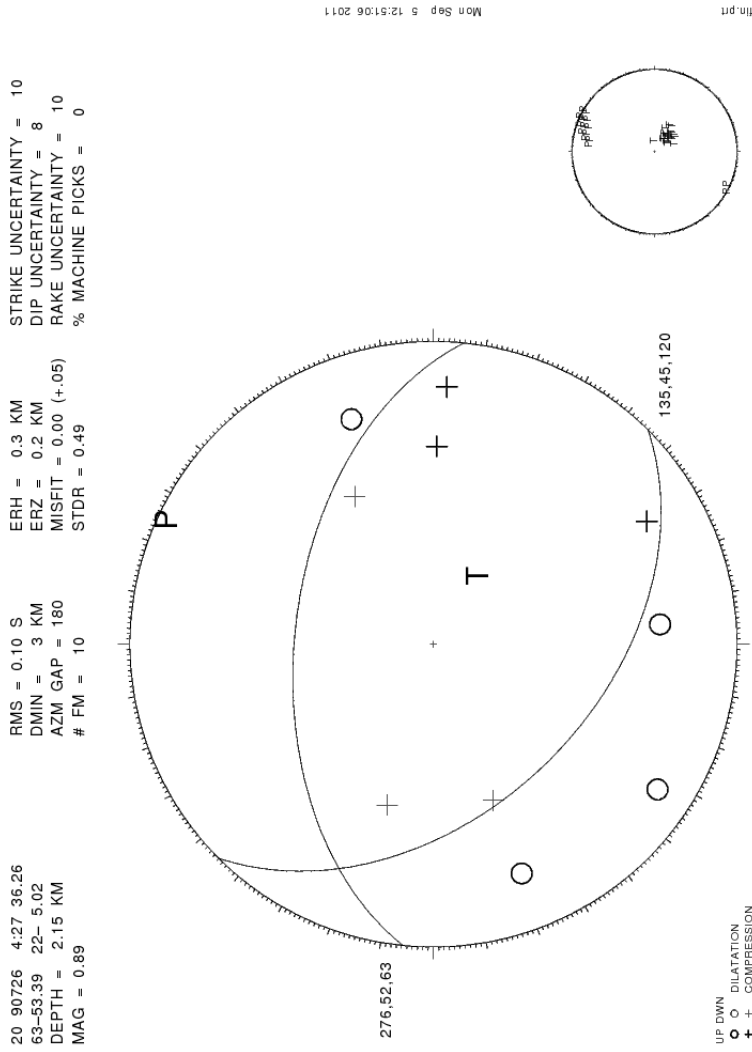
Figure 1.2: Example of focal mechanism solutions as plotted by FPFIT for an event recorded by instruments deployed in Krýsuvík from May till October 2009. The larger plot shows the lower-hemisphere projection with dilatational motion marked as open circles and compressional as plus signs. The letters P and T mark the location of the P- and T-axes, respectively. The smaller plot shows the distribution of possible orientations of P- and T-axes which are consistent with the data, allowing for uncertainty. The event took place on July 26, 2009 at 4:27:36.26 and has a reverse faulting mechanism, with a strike-slip component.
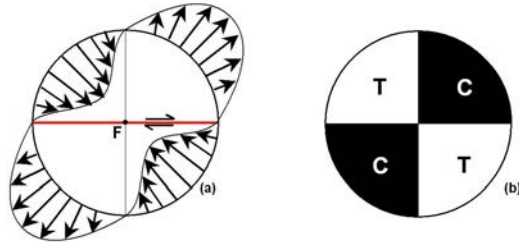
Figure 1.3: Example of a beach ball plot for a strike-slip event. The left plot shows the P-wave motion for the slip event and the right plot shows the associated beach ball. The P-wave motion plot and beach ball are identical for a right-lateral slip on a E-W trending vertical fault and a left-lateral slip on a N-S trending fault.

black and the dilatational sections left uncolored. Fig. 1.3 shows an example of the beach ball representation of a focal mechanism solution of a strike-slip event, and the associated P-wave motion.

1.1.2 Stress

Stress is defined as force per unit area, $\Delta \mathbf{F}/\Delta A$. We define the *stress vector* or *traction vector*, $\mathbf{T(n)}$, as the value of the stress when the surface area goes to zero,

$$\mathbf{T(n)} = \lim_{\Delta A \to 0} \frac{\Delta \mathbf{F}}{\Delta A} = T_1 \hat{\mathbf{x}} + T_2 \hat{\mathbf{y}} + T_3 \hat{\mathbf{z}}. \tag{1.1}$$

We follow the convention of setting compressive stress as positive. By imagining an infinitesimal cube surrounding a point in an elastic medium and considering the stresses at work on each side, we can develop a way to completely describe the stress at any point in the medium.

The stress vector $\mathbf{T(n)}$ acts on an arbitrary plane. Therefore, we can choose a plane which is parallel to one of the sides of our imagnary cube, e.g. the yz plane. The
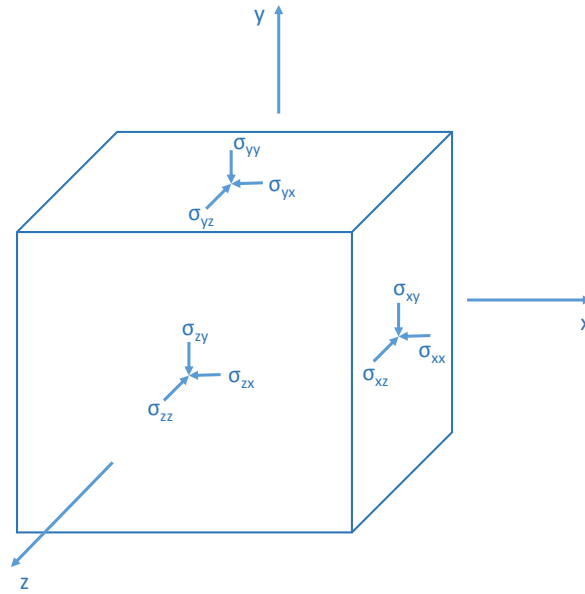
Figure 1.4: Infinitesimal cube in an elastic medium and the nine stress vectors which form the stress tensor.

stress components acting on this plane are defined by

$$\sigma_{xx} = \lim_{\Delta A_1 \to 0} \frac{\Delta F_1}{\Delta A_1} \tag{1.2}$$
$$\sigma_{xy} = \lim_{\Delta A_1 \to 0} \frac{\Delta F_2}{\Delta A_1}$$
$$\sigma_{xz} = \lim_{\Delta A_1 \to 0} \frac{\Delta F_3}{\Delta A_1}$$

where the first subscript corresponds to the direction of the normal to the plane being acted on by the force, and the second incex indicates the direction of the force. We also have

$$\Delta \mathbf{F} = \Delta F_1 \hat{\mathbf{x}} + \Delta F_2 \hat{\mathbf{y}} + \Delta F_3 \hat{\mathbf{z}}. \tag{1.3}$$

Similarly for each of the two other sides of the cube parallel to the xy and xz plane

we can define the three stress components acting on each surface. σ_{xx}, σ_{yy} and σ_{zz} are called *normal stresses* and σ_{xy}, σ_{xz} etc. are called *shear stresses*. In a state of equilibrium the nine stress vectors form the *stress tensor*:

$$\begin{pmatrix} \sigma_{xx} & \sigma_{xy} & \sigma_{xz} \\ \sigma_{yx} & \sigma_{yy} & \sigma_{yz} \\ \sigma_{zx} & \sigma_{zy} & \sigma_{zz}. \end{pmatrix} \tag{1.4}$$

The angular momentum must be in equilibrium too, requiring $\sigma_{xy} = \sigma_{yx}$, $\sigma_{xz} = \sigma_{zx}$ and $\sigma_{yz} = \sigma_{zy}$. Accordingly, the stress tensor is symmetric, reducing the number of independent components to six. At each point in a body, three mutually perpendicular planes exist on which no shear-stress components act (Lay and Wallace, 1995). This is called the principal coordinate system and is found by diagonalizing the stress tensor. The normals to the three planes are called the *principal stress axes*. The principal stress magnitudes are called σ_1, σ_2 and σ_3, where $\sigma_1 \geqslant \sigma_2 \geqslant \sigma_3$.

Focal mechanisms can be used to estimate the stress field in an area. Several methods have been developed to achieve this. They all assume a homogeneous stress field and that the fault slips in the direction of maximum resolved shear stress. Usually, only the direction of the principal stress axes can be estimated and the relative size of intermediate principal stress σ_2 compared to the maximum and minimum principal stress, σ_1 and σ_3. $R = (\sigma_1 - \sigma_2)/(\sigma_1 - \sigma_3)$ is used to estimate the relative size of the principal stresses. Gephart and Forsyth (1984) used a grid search method of stress models to find the one which required the smallest total rotation of all the fault planes that was needed to match the observed and predicted slip directions. The grid search method delivers a realistic error analysis and confidence limits for the preferred regional stresses. Angelier et al. (1982) employed a least squares method to solve the inverse problem. Their method took into account not only the errors

of the measured pitch of the slicken-slide, but also errors in the strike and dip of the plane. Michael (1984) linearized the problem by assuming that the length of the tangential traction vector on the fault plane is $|\tau| = 1$. Lund and Slunga (1999) based their work on the Gephart and Forsyth (1984) grid search method. Additionally, they used a range of focal mechanisms as input. This gives a measure of the uncertainty in the focal mechanism determination and a range of well-fitting fault plane solutions to account for the uncertainty during the stress tensor inversion. They also calculate the direction of maximum and minimum horizontal stress from the stress tensor (Lund and Townend, 2007). The stress tensor inversion from earthquake focal mechanisms requires several different types of events taking place on differently oriented planes in order to resolve the stress field. A drawback of using focal mechanisms to calculate the stress field is the ambiguity of possible nodal planes.

A Mohr diagram can be used to visualize the stress. In two dimensions, the expressions for the normal stress (σ) and shear stress (τ) acting on a plane oriented at angle θ to the direction of σ_1 in the principal coordinate systems look like this (Jaeger et al., 2007):

$$\sigma = \frac{(\sigma_1 + \sigma_2)}{2} + \frac{(\sigma_1 - \sigma_2)}{2} \cos 2\theta \tag{1.5}$$
$$\tau = \frac{-(\sigma_1 - \sigma_2)}{2} \sin 2\theta.$$

These equation describe a circle in the σ, τ-plane with center at the point ($\sigma = (\sigma_1 + \sigma_2)/2, \tau = 0$), and with radius ($\sigma_1 - \sigma_2$). Fig. 1.5 shows a Mohr diagram in two dimensions. The Mohr diagram can tell us the orientation of σ_1 in respect to
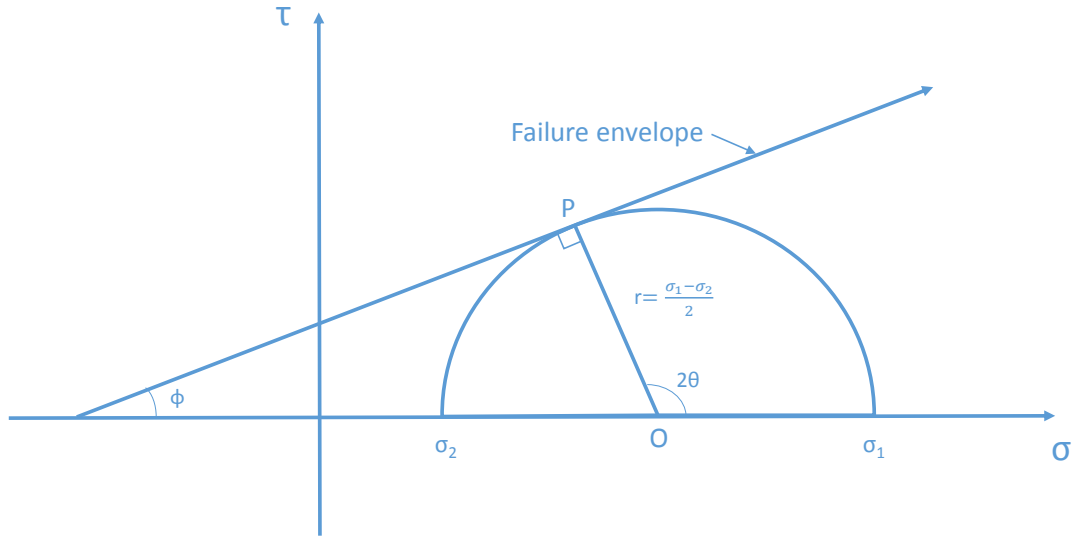
Figure 1.5: Mohr's circle in two dimensions. The failure envelope represents the magnitude of stress required for failure to occur. The radius of the Mohr circle is $r = (\sigma_1 - \sigma_2)/2$. The value of the angle from the σ-axis to line OP is 2θ, where θ is the angle which σ_1 makes with the strike of the fracture.

the strike of the fault. The angle from the σ axis to line OP is 2θ where θ is the angle between the direction of σ_1 and the strike. (See further discussion in Jaeger et al. (2007)). In three dimensions we can either visualize the stress tensor as circles on a Mohr diagram or an ellipsoid. The components of the traction vector lie on an ellipsoid with semi-axes σ_1, σ_2 and σ_3 (Lund, 2000)

$$\frac{t_x^2}{\sigma_1^2} + \frac{t_y^2}{\sigma_2^2} + \frac{t_z^2}{\sigma_3^2} = 1 \tag{1.6}$$

where $-\mathbf{t} = (\sigma_1 n_1, \sigma_2 n_2, \sigma_3 n_3)$ is the traction vector on a plane with normal $\mathbf{n}$ and $n_1^2 + n_2^2 + n_3^2 = 1$.

1.1.3 Moment tensor solution

The focal mechanism solutions described in section 1.1.1 exclude all volumetric change at the source. In order to reveal the volumetric change the full moment tensor must be calculated. The full moment tensor is composed of nine force couples for three-dimensional geometries (Lay and Wallace, 1995). Fig. 1.6 shows the nine fource couples. The moment tensor can be written as

$$M_{pq} = \mu A(\overline{u}_p v_q + \overline{u}_q v_p)$$ (1.7)

where μ is the shear modulus, A is the area and $\overline{u}_p$ is the average slip in the x_p direction on a plane with normal v_q in the x_q direction and vice versa (Aki and Richards, 2002). The moment tensor depends on source strength and fault orientation, and it characterizes all the information about the source that can be learned from observing waves whose wavelengths are much longer than the source dimensions. A moment tensor in the coordinate system defined in Fig. 1.6 looks like this for a point source of slip:

$$M = \begin{pmatrix} 0 & 0 & M_0 \\ 0 & 0 & 0 \\ M_0 & 0 & 0 \end{pmatrix}.$$ (1.8)
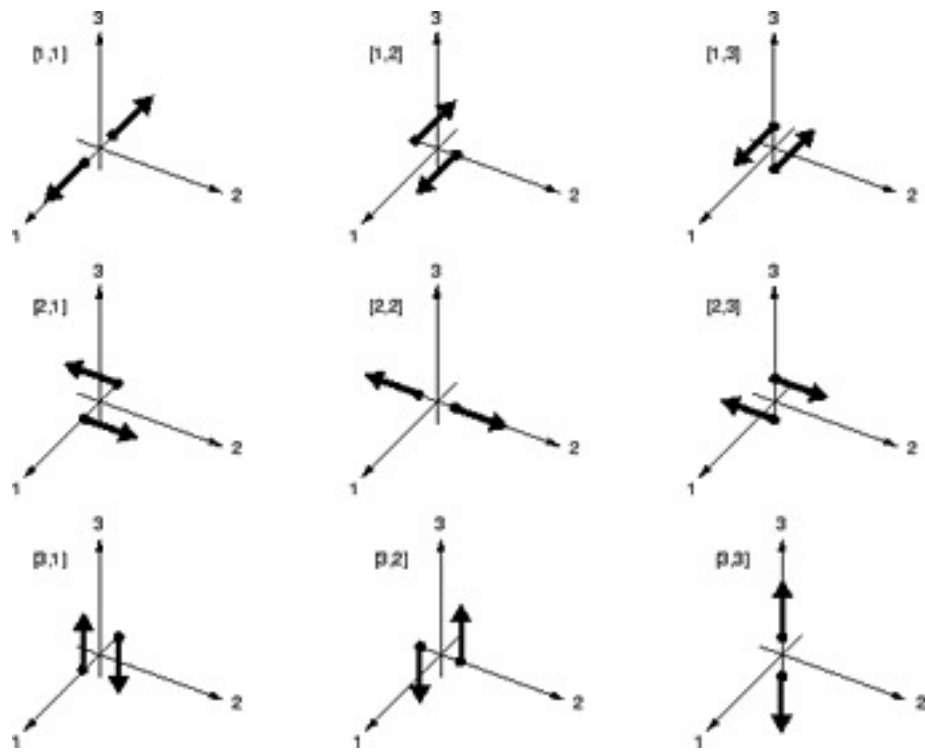
Figure 1.6: The nine couples composing the seismic moment tensor (United States Geological Survey).

1.2 Tomography and double-difference earthquake location

Seismic tomography is a method used to map, or image, the three-dimensional velocity structure inside the Earth. It is based on the principle that a particular seismic phase has a travel time, T, given by a path integral through the medium of

$$T = \int_s \frac{ds}{v(s)} = \int_s u(s)ds, \tag{1.9}$$

where $u(s)$ is the slowness $[1/v(s)]$ along the path (Lay and Wallace, 1995). By subdividing the medium into blocks and finding the slowness perturbations for different raypaths in each block, the velocity structure can be revealed. The best constrained blocks are the once with the highest number of traversing rays. The earthquake locations can either be fixed or the velocity structure and source location can be solved simultaneously. Earthquake tomography requires a dense receiver network and the resulting problem is usually mixed determined. The generalized inverse solution of the system is

$$\mathbf{m} = [\mathbf{G}^T\mathbf{G}]^{-1}\mathbf{G}^T\mathbf{d} \tag{1.10}$$

where $\mathbf{d} = \Delta T_i = T_{obs} - T_{pred}$ are the observed travel time residuals, $\mathbf{G} = l_{ij}$ is the path lengt of the i-th ray in the j-th block, and $\mathbf{m} = \Delta u_j$ is the slowness perturbation in the j-th block. By calculating a resolution matrix for the problem we can estimate how well the model can be reconstructed if the data and model parameterization are perfect. The velocity perturbation in blocks with few or none traversing rays can not be determined adequately, and the resolution matrix helps identifying those regions.

The tomography method relies on accurately estimated earthquake locations. Two factors have the biggest effect on location uncertainty: errors in arrival time measurements and velocity model errors. An earthquake location can be absolute or relative. Relative earthquake location methods can improve the uncertainty estimates by a few orders of magnitude (Husen and Hardebeck, 2010). Relative earthquake location methods assume that the hypocentral distance between two earthquakes is small compared to the event-station distance. Consequently the two rays travel almost identical paths to the common receiver. The difference in travel times originates from the small difference in source location. The travel time difference can be accurately identified with waveform cross-correlation. The relative location between earthquakes can be calculated with errors of a few meters to a few tens of meters when using cross-correlation (Waldhauser and Ellsworth, 2000).

Waldhauser and Ellsworth (2000) developed the double-difference method which determines hypocenter locations of earthquakes over large distance with high resolution. It is based on comparing the observed and theoretical travel time differences of two events:

$$dr_k^{ij} = (t_k^i - t_k^j)^{obs} - (t_k^i - t_k^j)^{cal}. \tag{1.11}$$

Here dr_k^{ij} is the residual and t_k^i and t_k^j are the travel times of events i and j at station k. Observed travel times can either be absolute travel times from measured arrival times or cross-correlation relative travel-time differences. To reach this conclusion, Waldhauser and Ellsworth (2000) start with:

$$T_k^i = \tau^i + \int_i^k u ds, \tag{1.12}$$

where T is the arrival time for earthquake i to seismic station k, τ is the origin time of event i, u is the slowness field and ds is an element of path length. Usually, a

Taylor series expansion is used to make this nonlinear problem linear. This gives us a problem where the travel-time residuals, r, for an event i are linearly related to perturbations, $\Delta\mathbf{m}$, to the four current hypocentral parameters for each observation k:

$$\frac{\partial t_k^i}{\partial\mathbf{m}}\Delta\mathbf{m}^i = r_k^i, \qquad (1.13)$$

where $r_k^j = (t^{obs} - t^{cal})_k^i$, t^{obs} and t^{cal} are the observed and theoretical travel time, respectively, and $\Delta\mathbf{m}^i = (\Delta x^i, \Delta y^i, \Delta z^i, \Delta\tau^i)$. To be able to use cross-correlation travel-times, which measures differences between events, $(t_k^i - t_k^j)^{obs}$, we have to take the difference between equation 1.13 for a pair of events (Fréchet (1985), as cited by Waldhauser and Ellsworth (2000)):

$$\frac{\partial t_k^{ij}}{\partial\mathbf{m}}\Delta\mathbf{m}^{ij} = dr_k^{ij}, \qquad (1.14)$$

where $\Delta\mathbf{m}^{ij} = (\Delta dx^{ij}, \Delta dy^{ij}, \Delta dz^{ij}, \Delta d\tau^{ij})$ is the change in the relative hypocentral parameters between the two events, and the partial derivatives of t with respect to $\mathbf{m}$ are the components of slowness vector of the ray connecting the source and receiver measured at the source. The slowness vector is only constant for events that are close together. Therefore, an adjustment has to be made to be able to include events which are far apart. This can be done by using the appropriate slowness vector and origin time term for each event when taking the difference between equation 1.13:

$$\frac{\partial t_k^i}{\partial\mathbf{m}}\Delta\mathbf{m}^i - \frac{\partial t_k^j}{\partial\mathbf{m}}\Delta\mathbf{m}^j = dr_k^{ij}. \qquad (1.15)$$

Written out in full:

$$\frac{\partial t_k^i}{\partial x}\Delta x^i + \frac{\partial t_k^i}{\partial y}\Delta y^i + \frac{\partial t_k^i}{\partial z}\Delta z^i + \Delta\tau^i - \frac{\partial t_k^j}{\partial x}\Delta x^j - \frac{\partial t_k^j}{\partial y}\Delta y^j - \frac{\partial t_k^j}{\partial z}\Delta z^j - \Delta\tau^j = dr_k^{ij} \quad (1.16)$$

The partial derivatives of the travel times, t, for events i and j, with respect to their locations (x, y, z) and origin times (τ), respectively, are calculated for the current hypocenters and the location of the station where the k-th phase was recorded. $\Delta x, \Delta y, \Delta z$ and $\Delta \tau$ are the changes required in the hypocentral parameters to make the model better fit the data (Waldhauser and Ellsworth, 2000). This can be combined into a system of linear equation for all hypocentral pairs of a station, for all stations:

$$\mathbf{WGm} = \mathbf{Wd} \tag{1.17}$$

where $\mathbf{G}$ defines a matrix of size $M \times 4N$ (M, number of double-difference observations; N, number of events) containing the partial derivatives, $\mathbf{d}$ is the data vector containing the double-differences, $\mathbf{m}$ is a vector of length $4N$, $[\Delta x, \Delta y, \Delta z, \Delta T]^T$, containing the changes in hypocentral parameters that are to be determined, and $\mathbf{W}$ is a diagonal matrix to weight each equation (Waldhauser and Ellsworth, 2000).

Zhang and Thurber (2003) developed a double-difference tomography method which simultaneously determines the relative and absolute event locations and the velocity structure. Their code *tomoDD* is based on the double-difference location code *hypoDD* written by Waldhauser (2001). *tomoDD* was used to relocate all the events in the Krýsuvík and Fagradalsfjall areas recorded by a dense network deployed in the area from May till October, 2009 (Franco, 2013).

2 Introduction

Iceland is a volcanic island straddling the Mid-Atlantic ridge in the North Atlantic Ocean. It is shaped by the interaction of a mantle plume with an oceanic spreading ridge. Due to the presence of the mantle plume the plate boundary in Iceland is considerably oblique compared to the plate motion. The segment of the Mid-Atlantic ridge which connects with Iceland in the Southwest is called the Reykjanes Ridge. It comes onshore in the southwestern part of the island, on the Reykjanes Peninsula (RP). The volcanic zones in Iceland, the location of the RP and the direction of plate motion are shown on the inset of Fig. 2.1. The RP plate boundary is an oblique spreading rift, striking N80°E compared to the spreading direction of N102.1±1.1°E (DeMets et al., 1994). The RP plate boundary splits into the South Iceland Seismic Zone (SISZ) and the Western Volcanic Zone (WVZ) at the Hengill Triple Junction. The SISZ is an E-W oriented transform zone where the left lateral shear is accommodated by N-S striking right-lateral faults, while the rifting at the WVZ is believed to be slowly dying out and the spreading motion is migrating to the Eastern Volcanic Zone (EVZ) (LaFemina et al., 2005).

The main tectonic features on the Reykjanes Peninsula are NE-SW trending volcanic fissures, hyaloclastite ridges and normal faults and N-S trending right-lateral strike-slip faults. Five different volcanic systems with associated fissure swarms are
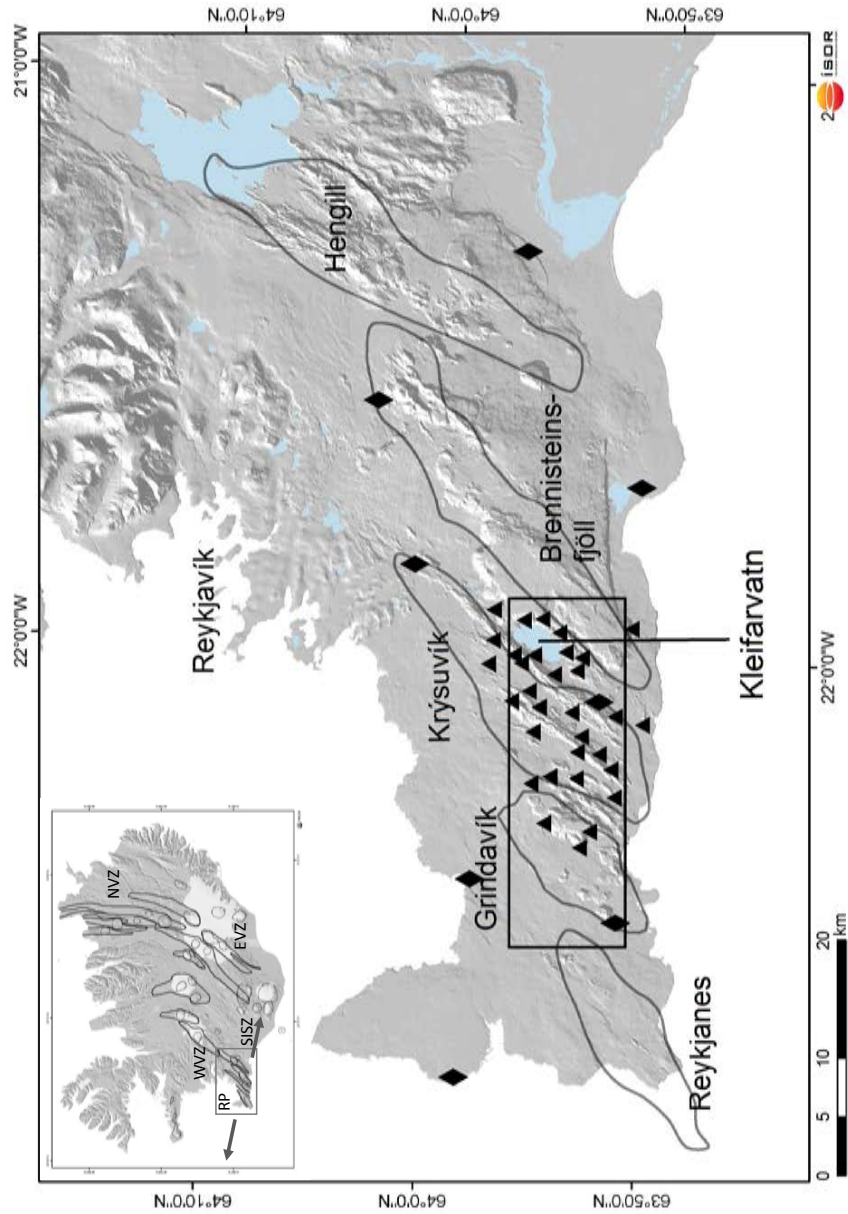
Figure 2.1: Volcanic fissure swarms on the Reykjanes Peninsula as described by Jakobsson et al. (1978) drawn with dark gray lines. The locations of stations deployed during the measurement period are marked as black triangles. Stations from the SIL-network are marked as black diamonds. The box outlines the area displayed in Fig. 3.2. The inset shows the volcanic zones in Iceland. WVZ = Western Volcanic Zone, SISZ = South Iceland Seismic Zone, EVZ = Eastern Volcanic Zone, NVZ = Northern Volcanic Zone and RP = Reykjanes Peninsula. The two arrows show the direction of plate spreading according to NUVEL-1A (DeMets et al., 1994).

identified on the peninsula (Fig. 2.1): Reykjanes, Grindavík, Krýsuvík, Brennisteins-fjöll and Hengill (Jakobsson et al., 1978). Reykjanes and Grindavík are sometimes grouped together as one volcanic system (Saemundsson, 1978). Each system consists of increased volcanic production and a fissure swarm as well as a high temperature geothermal field. Here, five geothermal fields are recognized: Reykjanes, Eldvörp-Svartsengi (part of the Grindavík system), Krýsuvík, Brennisteinsfjöll, and Hengill. Three of them are currently being exploited: Reykjanes, Svartsengi, and Hengill. Seismic and magmatic activity appears to be periodic, with seismicity increasing every thirty-forty years and magmatic episodes every thousand years (Einarsson, 2008).

The Krýsuvík geothermal field is the main focus of this paper. Results from a seismic survey in the area in 2005 revealed a low P-wave velocity anomaly southwest of Lake Kleifarvatn (Geoffroy and Dorbath, 2008). In light of this result and in hope of enhancing the knowledge of the Krýsuvík geothermal system, a large project involving scientists from the French Geoflux project and the Iceland GeoSurvey was launched. The project, called HYDRORIFT, was supported by the Geothermal Research Fund (GEORG) and the energy company HS Orka, based in Iceland. A dense seismic network was operated in the area from May to October 2009. The location of the seismic stations can be viewed in Fig. 2.1. They are also listed in Table 2.1 along with stations from the Iceland Meteorological Office network (SIL) supplementing the data. The network was deployed during an active deformation period in Krýsuvík accompanied by high levels of seismicity. Consequently a large data set was obtained. Our French coworkers produced detailed tomography of the area, confirming the location of the low P-wave velocity anomaly southwest of Lake Kleifarvatn (Franco, 2013). Additionally ISOR developed a 3D model of the resistivity structure in the area from magnetotelluric (MT) data (Hersir et al., 2013).

Table 2.1: Location and elevation (H) information of seismic stations used to gather data for the research. Stations identified with three uppercase letters are from the Iceland GeoSurvey, stations with names starting with capital G belonge to Geoflux and stations identified with three lowercase letters are from the Icelandic Meteorological Office network (SIL).

Stn.	Lat. [°]	Lon. [°]	H [m]	Stn.	Lat. [°]	Lon. [°]	H [m]
KLN	63.93815	-21.94053	161.45	G70	63.92700	-22.22280	250.60
KLV	63.91315	-22.03261	162.32	G72	63.91270	-22.20880	238.37
KLE	63.91050	-21.95963	158.00	G73	63.96070	-21.97770	257.87
NUP	63.89295	-22.16410	176.45	G74	63.96350	-22.01900	173.46
HRU	63.93146	-22.06257	217.57	G75	63.94450	-22.00200	325.36
HAM	63.86684	-22.19215	125.22	G76	63.89600	-22.02420	263.10
NAT	63.88062	-22.30049	101.57	G80	63.85570	-21.94780	150.33
ODD	63.92733	-22.13328	184.43	G87	63.86530	-22.10020	192.81
VIG	63.89026	-22.13764	166.60	G89	63.93870	-22.01520	323.73
DJU	63.92357	-22.08989	215.00	G90	63.94470	-22.08120	268.03
FAD	63.96118	-21.92524	180.33	G93	63.87620	-22.16670	211.00
SAN	63.88744	-22.32909	77.91	G95	63.86330	-22.24020	174.55
FAF	63.91552	-22.29039	109.82	kri	63.87811	-22.07623	130.00
G05	63.92420	-22.93720	412.93	vog	63.96967	-22.39283	12.00
G06	63.90500	-21.99300	262.24	grv	63.85716	-22.45583	52.00
G31	63.89850	-22.09680	272.70	vos	63.85279	-21.70359	12.00
G36	63.84430	-22.11230	129.55	nyl	63.97370	-22.73790	11.00
G37	63.89270	-22.00130	294.46	kas	64.02290	-21.85200	108.00
G48	63.89270	-22.21020	225.60	san	64.05601	-21.87013	260.00
G49	63.92900	-22.00030	259.01	bja	63.94622	-21.30287	58.00

3 Seismicity on the Reykjanes Peninsula

The first seismometer was installed in Iceland in 1909 (Einarsson and Björnsson, 1987). It was removed in 1914 (Tryggvason, 1973). The seismometer was reinstalled in 1925 and seismicity in Iceland has been continuously recorded since then (Einarsson and Björnsson, 1987). The seismic activity on the Reykjanes Peninsula seems periodic with episodes of high activity occurring approximately every thirty to forty years. High seismicity was observed in 1929-1935, 1967-1973, and in 2000 (Einarsson, 2008). The seismicity delineates a zone that trends approximately N80°E along most of the peninsula, bending towards southwest at the transition to the off-shore Reykjanes Ridge (Keiding et al., 2008). Most earthquakes occur on the central RP between 4-6 km depth, but reaching down to 7-8 km depth. Keiding et al. (2008) and Einarsson (1991) observe a systematic change in the pattern of seismicity along the Reykjanes Peninsula. The western part of the peninsula is characterized by swarm activity and rare mainshock-aftershock sequences while in the eastern part mainshock-aftershock sequences are more frequent. The central part of the peninsula, where Krýsuvík is located, acts as a transition between the two.

The largest instrumentally recorded event on the RP took place in 1929 on a 10

km long N-S oriented strike-slip fault called the Hvalhnúkur fault (Erlendsson and Einarsson, 1996). It is estimated to have been a $M_S = 6.2$ earthquake (Tryggvason, 1973). The Hvalhnúkur fault is located east of lake Kleifarvatn and has been active on several occasions since 1929 (Keiding et al., 2008). Other significant events include three triggered events on three different faults following a $M_W = 6.5$ event in the SISZ on June 17th, 2000 (Pagli et al., 2003). The first event occurred near the northern end of the Hvalhnúkur fault, the second event near Lake Kleifarvatn, and the last one was located near Núphlíðarháls. The first two events were probably dynamically triggered by surface waves from the June 17th main shock (Árnadóttir et al., 2004). Additionally a $M_W = 5.1$ earthquake occurred on August 23rd, 2003, rupturing a N-S oriented strike-slip fault beneath Sveifluháls, west of Lake Kleifarvatn (Keiding et al., 2008; Pagli et al., 2003). An increase in activity was also observed following an earthquake doublet in the SISZ in May 2008. The earthquake doublet had an estimated composite moment magnitude of $M_W = 6.1 - 6.2$ (Decriem et al., 2010; Hreinsdóttir et al., 2009).

3.1 Seismicity and deformation

Early in 2009 a period of uplift started in the Krýsuvík geothermal area (Michalczewska et al., 2012). The uplift was observed at GPS stations in the area (Fig. 3.1). The uplift continued until the fall of 2009 when the area started subsiding. Another period of uplift started in April 2010 and lasted until the beginning of 2012 when the area began to subside again. An increase in seismic activity was detected during the uplift sequences. During the period of uplift in 2009 (from May to October) a seismic network of 32 stations was in operation in the Krýsuvík and Kleifarvatn area. The network recorded over 10,000 events during this time. The regional SIL-

Figure 3.1: Displacement on GPS station KRIV located south of Krýsuvík. Components are North, East and Up. Two sequences of rapid displacement episodes are observed, most noticable on the North component. The two sequences took place in 2009 and 2011. The total amount of uplift was $\sim$ 20 mm on the North component. (Hreinsdóttir and Michalczewska).

network operated by the Icelandic Meteorological Office recorded a few swarms in the area before the additional seismic network was fully deployed.

3.2 Seismicity in Krýsuvík, May - October 2009

Over 10,000 events were detected in the research area in the period from May till October 2009. Of the 10,000 detected events 6,100 were manually picked and the computer software tomoDD (Zhang and Thurber, 2003) used to relocate the events and develop a 3D velocity model of the crust (Franco, 2013). Fig. 3.2 shows the locations of the 2,800 best defined relocated events as well as an E-W depth profile of the hypocenters. The main active areas were at Fagradalsfjall in the west and at Krýsuvík in the east. Both areas have previously been active (Hjaltadóttir and

Vogfjörð, 2006a; Keiding et al., 2009). The observed activity is characterized by intense swarms in between quieter periods of scattered seismicity. From Fig. 3.3 three main swarms can be identified. The first and most intensive swarm took place in Fagradalsfjall on May 29th and 30th. The activity was scattered with a small indication of N-S striking faults (Fig. 3.2). Twenty days later the activity picked up to the southwest of Lake Kleifarvatn, migrating north and east. This activity delineates at least three N-S striking faults. The last swarm occurred around August 1st, delineating a N-S striking fault in northern Móhálsadalur. Other smaller swarms also outline N-S striking faults. The hypocenter depth profile in Fig. 3.2 clearly shows that the delineated faults all have a dip close to 90°. The majority of earthquakes are located at a depth between 1.5 km and 4 km (>70%). The epicenters in the Fagradalsfjall area are at a greater depth compared to the Krýsuvík area. In the Krýsuvík area, west of Lake Kleifarvatn, an updoming in the earthquake hypocenter depth distribution is evident. The center of the dome correlates with signs of geothermal activity on the surface. This concurs with the findings of Keiding et al. (2009), who found the shallowest earthquake activity of events taking place from 1997-2006 to be in the central Krýsuvík area. Furthermore, this correlates with the locations of a low P-wave velocity anomaly detected in the tomography results (Franco, 2013) as well as a low resistivity anomaly observed in 3D interpretations of magnetotelluric resistivity data (Hersir et al., 2013).
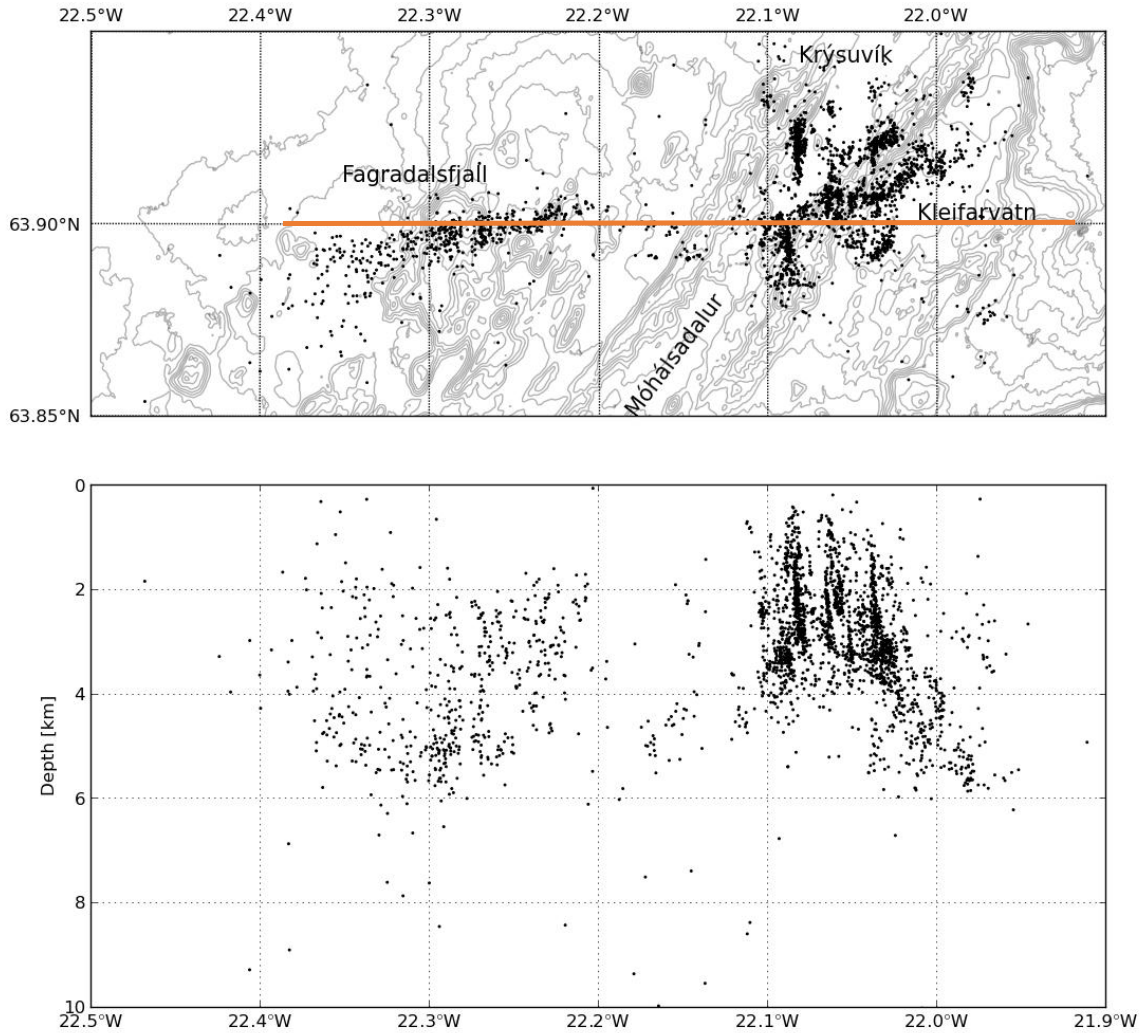
Figure 3.2: Map and depth profile of 2,800 relocated events in Fagradalsfjall and Krýsuvík May-October 2009. The activity delineates several N-S striking, steeply dipping faults. The events are shallower in the Krýsuvík area and show signs of an updoming which correlates with geothermal activity on the surface, and may indicate a change in depth to the brittle-ductile boundary. The orange line marks the location of cross sections presented in Fig. 3.4.
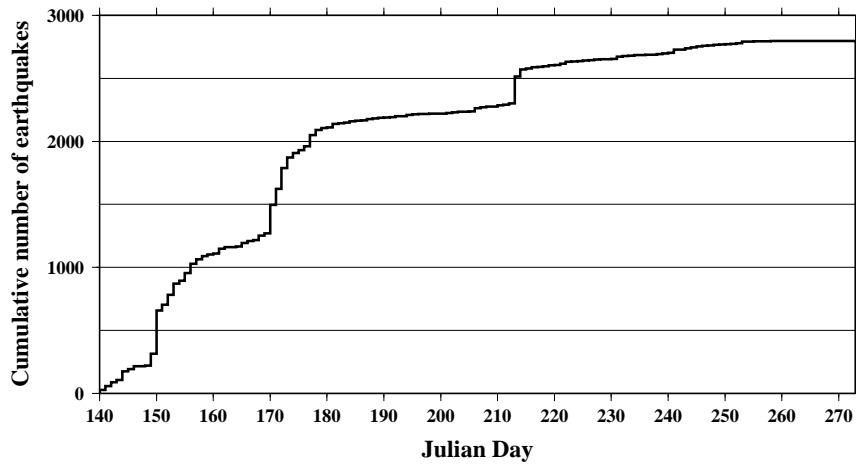
Figure 3.3: Cumulative number of relocated earthquakes May-Oct. 2009. Three main swarms are detected, on May 29-30 (julian day 150-151), June 19-21 (julian day 170-172) and August 1-2 (julian day 213-214).

3.3 Seismicity and resistivity

Franco (2013) confirmed the location of a low P-wave velocity anomaly in the Krýsuvík area. The anomaly had been observed in tomography results from data collected in 2005 (Geoffroy and Dorbath, 2008). A vertical section running E-W through Krýsuvík and the southern part of Lake Kleifarvatn and showing the P-wave velocity calculated for the data collected in 2009 can be seen in Fig. 3.4. The P-wave anomaly is seen at 5-8 km depth. Earthquake activity decreases dramatically in the low P-wave volume. The location of a low resistivity anomaly observed in the Krýsuvík area in 3D modelling of magnetotelluric data correlates with the location of the low P-wave velocity anomaly (Hersir et al., 2013). However, the resistivity anomaly is shallower, mainly occupying depths of 1.5-5 km.
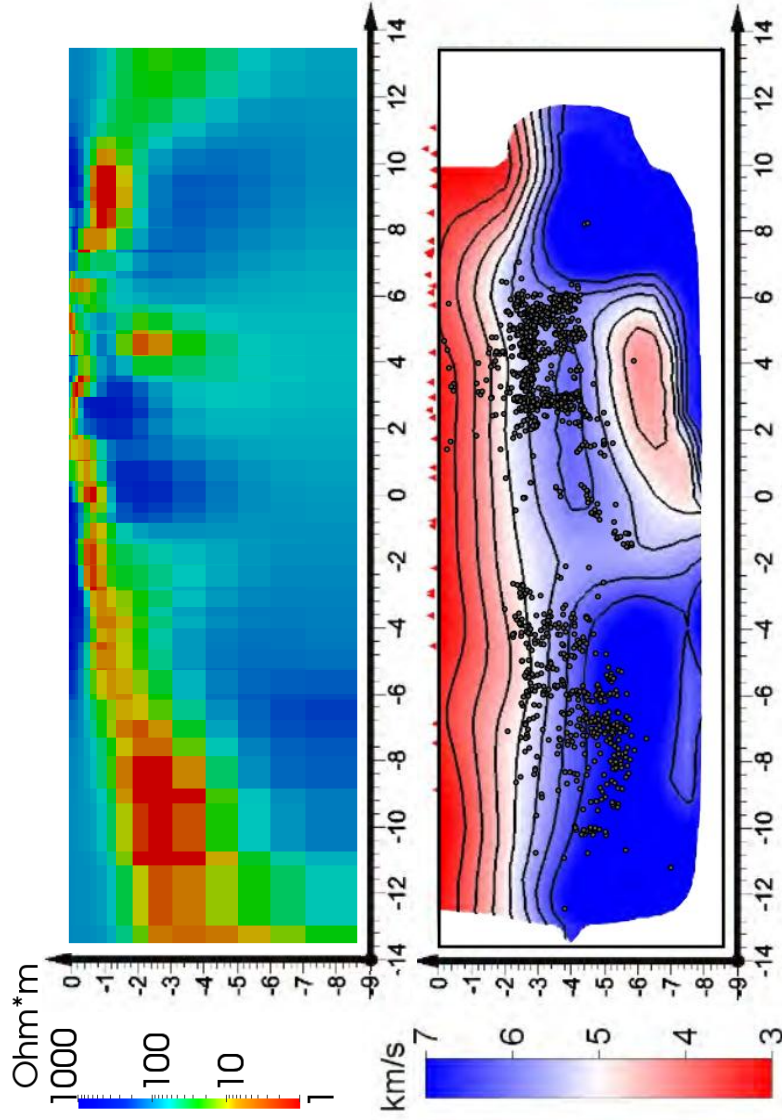
Figure 3.4: Resistivity and velocity structure beneath Krýsuvík. The location of the cross sections can be seen in Fig. 3.2. Top: Vertical cross-section from a 3D inversion of magnetotelluric data (Hersir et al., 2013). A low resistivity anomaly can be seen at 1.5-5 km depth, approximately beneath the Krýsuvík geothermal area. Bottom: Vertical cross-section of the P-wave velocity model based on data recorded from May till October 2009 (Franco, 2013). A low P-wave velocity anomaly can be seen at around 5-8 km depth. Earthquake hypocenters 500 m to the south and north of the cross section are marked as dots and network stations as red triangles.

3.4 The brittle-ductile boundary
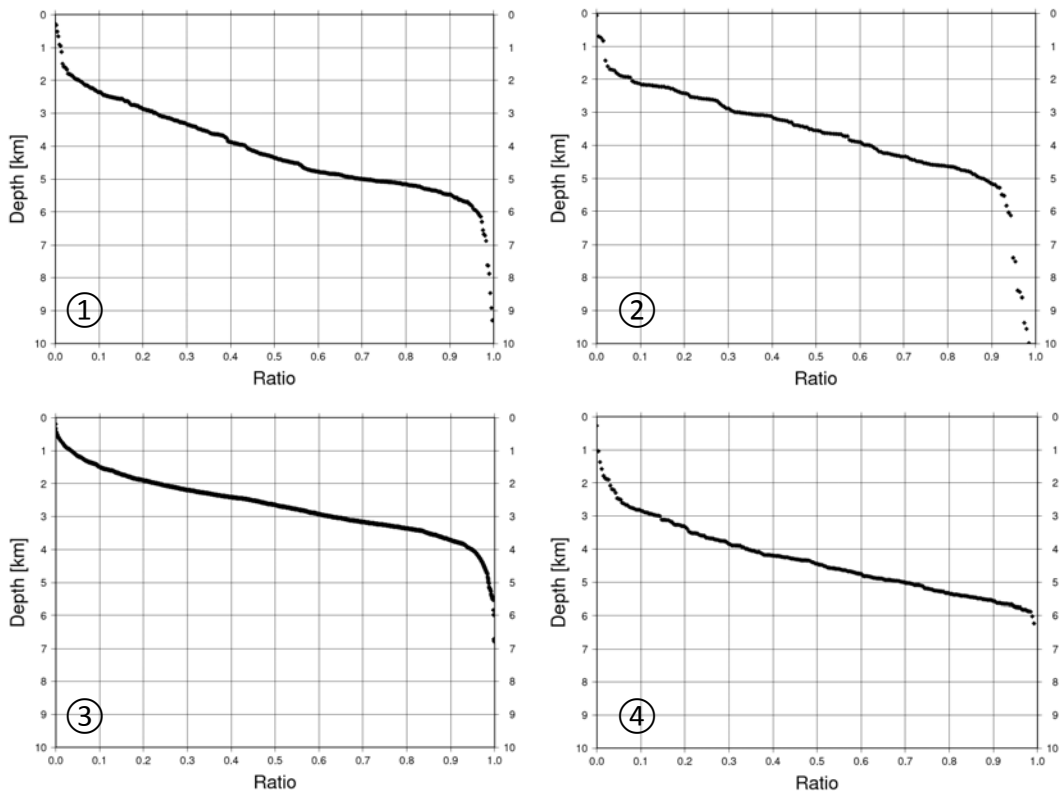
Figure 3.5: Cumulative depth distribution for four different sectors in Fagradalsfjall and Krýsuvík area. The division can be viewed in Fig. 3.6. A distinct change or fall-off can be seen between the ratios of 0.9 and 1.0 in all the graphs.

The cumulative depth distribution of earthquakes for four sectors of the data (divided by longitude) reveals a clear trend in depth distribution. Fig. 3.5 shows the results for the four different sectors. A distinct change or fall-off can be seen between the ratios of 0.9 and 1.0 in all the graphs. Specifically, the depth in different sectors is as follows: 1) 95% of events above 5.8 km; 2) 92% of events above 5.3 km; 3) 95% of events above 4.0 km; and 4) 98% above 5.9 km. In Fig. 3.6 the depth for each sector is drawn as a thick black line with the earthquake hypocenters in the background as black dots. Sector 3, where the most activity is located stands out.

95% of the activity in this sector is above 4.0 km, while in the other areas it ranges from 5.3-5.9 km. This suggests that the brittle-ductile boundary domes up in this area which lies beneath the Krýsuvík geothermal field.
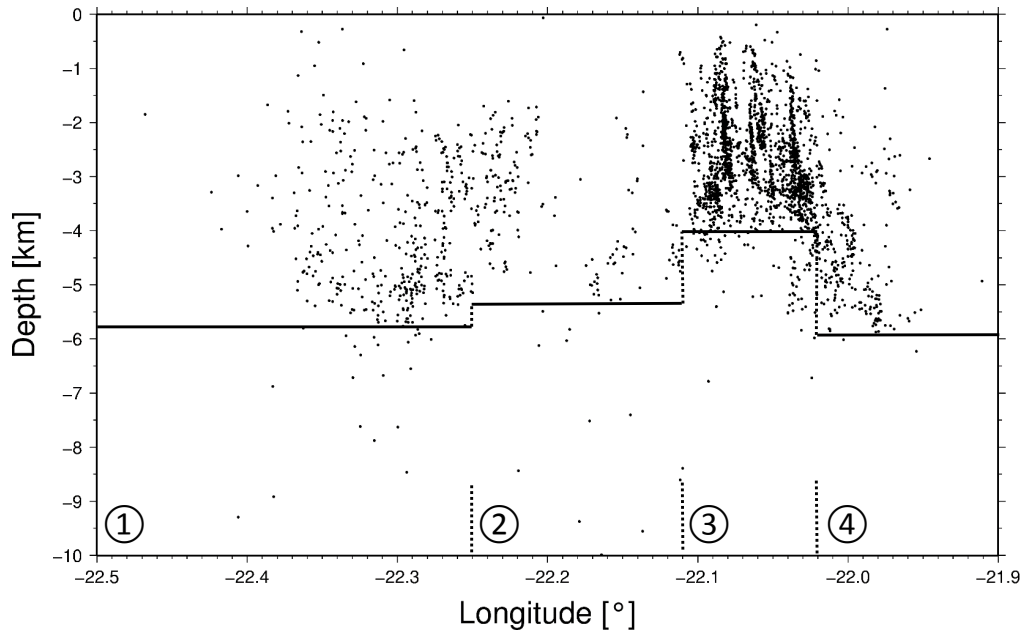
Figure 3.6: Depth profile of hypocenters of relocated earthquakes in Fagradals-fjall and Krýsuvík with a thick black line indicating the depth above which the majority of earthquakes are located. The depth varies between the four defined sectors, ranging from 5.9 km to 4.0 km. The change in depth may indicate a variation in depth to the brittle-ductile boundary.

4 Focal mechanisms

4.1 Methods and results

Focal mechanisms were calculated for 1,643 events using the computer program FPFIT (Reasenberg and Oppenheimer, 1985). The FPFIT program computes double-couple fault-plane solutions from P-wave first motion data using a grid search method. For each double-couple source model obtained, FPFIT formally estimates the uncertainty in the model parameters (strike, dip, and rake). Only events with ten polarities or more were considered for calculations. Of these the best deter-mined solutions (with uncertainty $< 20°$ for strike, dip, and rake) were used for further analysis, in total 1,063 events. 138 events are located in the Fagradalsfjall area and 923 in the Krýsuvík area.

The focal mechanisms can be categorized into four different groups depending on which of the P, B, or T axis is closest to vertical. When the P or B axis lies within 30° from vertical the event is classified as normal or strike-slip, respectively, and if the T axis lies within 40° from vertical it is classified as a reverse faulting event. If none of the axes are within the defined angular distance from vertical the event is either classified as an oblique faulting event or a pure dip-slip on a vertical fault. In the

total set of focal mechanisms 43% are oblique, 22% are strike-slip, 10% are normal, and 22% are reverse faulting with only 3% representing dip-slip on vertical faults (see Table 4.1). The ratio for the Krýsuvík subset resembles the results of the total dataset, with 43% oblique faulting, 23% strike-slip, 11% normal, 20% reverse, and 3% dip-slip. The Fagradalsfjall subset differs significantly. The oblique, strike-slip, and dip-slip events have similar ratios: 40% oblique, 20% strike-slip, and 3% dip-slip while the normal faulting events comprise 2% of the total subset and reverse faulting 35%. An evaluation of dip of the different focal mechanism solutions reveals that a majority of oblique and strike-slip events take place on steep faults while normal and reverse faulting events occur on shallower-dipping faults with dip $\sim 50°$ (see Fig. 4.1). Keiding et al. (2009) found when analyzing earthquake data from the RP from 1997-2006 that 50-60% of the mechanisms were oblique. In the Fagradalsfjall area they determined that most events were strike-slip or normal faulting with only 5-6% reverse mechanisms (including oblique events with a plunge of the T-axis less than 60°). There is a striking difference in the percentage of reverse mechanism in Fagradalsfjall observed by Keiding et al. (2009) when compared to our results (5-6% vs. 35%). In the Krýsuvík area however, Keiding et al. (2009) found the proportion of reverse mechanism to be 21-26% (including oblique events), closer to our result of 20%. The Icelandic Meteorological Office (IMO) generously provided us with data

Table 4.1: Classification of focal mechanisms for the Fagradalsfjall area, Krýsuvík area and the total set of fault plane solutions. Focal mechanisms are categorized by which of the P, T or B axis is closest to vertical (see text).

	Fagradalsfjall	**Krýsuvík**	**Whole dataset**
Oblique	40%	43%	43%
Strike-slip	20%	23%	22%
Normal	2%	11%	10%
Reverse	35%	20%	22%
Dip-slip	3%	3%	3%
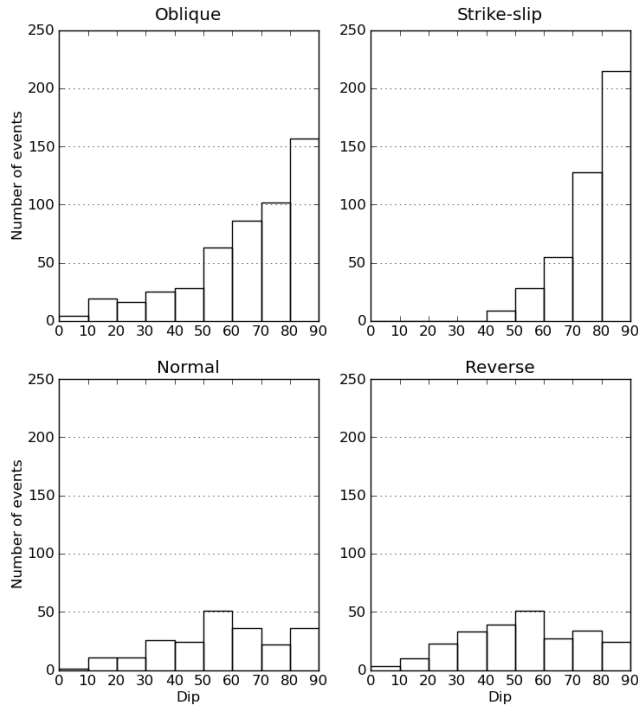
Figure 4.1: Histograms showing the distribution of dip for different focal mechanism solutions. Oblique and strike-slip events generally take place on steep faults. Normal and reverse faulting events largely occur on planes with less dip.

for events measured on their regional seismic network from 1994-2011 in Þeistareykir and Bjarnaflag geothermal areas in the Northern Volcanic Zone. In order to be able to compare the areas we catagorized the focal mechanisms of these events by the direction of P, B, and T axes in the same way as our data from Krýsuvík and Fagradalsfjall. The results show diverse faulting events. In both Þeistareykir and Bjarnaflag more than half of the events are oblique (62% and 56%, respectively) and around 20% are strike-slip events. However, the areas differ when it comes to normal and reverse faulting events. In Þeistareykir 12% of the events were normal faulting events, but only 5% of the Bjarnaflag events register as normal faulting. 9% of the events in Þeistareykir were reverse but 18% of the events in Bjarnaflag were reverse. Bjarnaflag resembles Krýsuvík in the ratio of reverse faulting events. We must bear in mind, that the events in Þeistareykir and Bjarnaflag were recorded over a period of 18 years on stations of the regional seismic network of the Icelandic Meteorological Office.

Fig. 4.2 shows the distribution of focal mechanisms for several subsets of the Krýsu-vík dataset on ternary diagrams. The events were grouped together in subsets depending on location in space and time, based on faults discerned in the relocated dataset (see Fig. 3.2). One of these subsets, number 3, was further divided into three smaller sets (3a-c). Subsets 3a-c are all a part of the same swarm taking place in northern Núphlíð in a two day period. The events with calculated focal mechanisms are not relocated. The ternary diagrams show focal mechanisms plotted on an equal-area projection of an octant (Lund, 2012). Strike-slip events fall in the top corner, normal faulting events in the lower left corner and reverse faulting events in the lower right corner. Oblique events are presented in the center of the diagram. Thin lines show the 30° plunge angle for strike-slip and normal events and 40° plunge angle for reverse faulting events. The ternary diagram in the top right corner of Fig. 4.2 shows the distribution of focal mechanism solutions for all the events in the Krýsuvík area. It reveals that the recorded events cover the whole spectrum of focal mechanisms solutions. All of the subsets have varied focal mechanisms solutions. Subsets 2 and 10 display the most scattering of focal mechanism solutions, covering most of the ternary diagram. Subsets 7, 3c and 6 are mostly oblique while subsets 1, 4 and 5 show a mixture of reverse and oblique faulting, with subset 1 moving into strike-slip faulting. Subsets 3b and 8 have mechanisms classified as strike-slip, normal and reverse faulting events with fewer oblique events. Subset 3a shows mostly normal faulting and reverse faulting events while subset 9 features mainly strike-slip events mixed with oblique events containing a strike-slip factor.
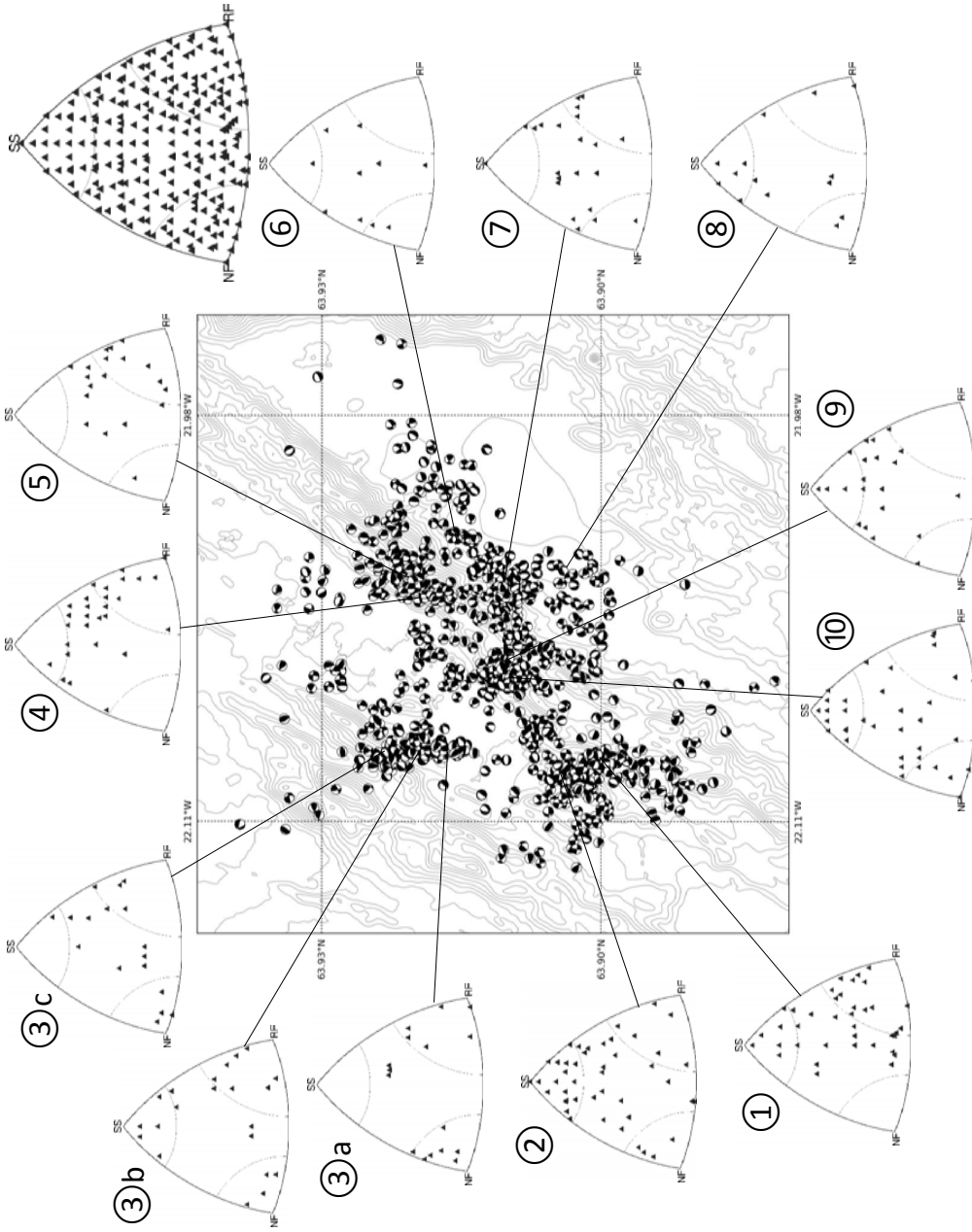
Figure 4.2: Ternary diagrams of the twelve subsets of the Krýsuvík area events (numbered 1-10). Events are mapped as beachballs, the visual representation of focal mechanism solutions. On the perimeter are ternary diagrams of the focal mechanism distributions of the respective subsets. Strike-slip events fall in the top corner of the diagram, normal events in the lower left corner and reverse events in the lower right corner. The top right ternary diagram (un-numbered) shows the focal mechanism distribution for the whole data set. It shows clearly the diversity of calculated focal mechanisms.

4.2 Swarm in northern Núphlíð

The swarm in northern Núphlíð (3a-c in Fig. 4.2) occurred predominantly on 31.7-1.8, 2009. It clearly delineates a N-S trending fault with activity limited to depths of 1-3 km. Focal mechanism solutions were calculated for 78 events in the swarm. Fig. 4.3 shows the results as lower hemisphere projections. Fig. 4.3A shows all 78 mechanisms while B-E show mechanisms catagorised by which of the P, B or T axis is closest to vertical (see further explanation in previous section). The division reveals that 35% of the events are oblique (27% oblique, 8% dip-slip events; see Fig. 4.3B), only 8% are strike-slip (Fig. 4.3C), 26% are normal (Fig. 4.3D) and 32% are reverse (Fig. 4.3E). The oblique, normal and reverse groups have distinct yet different strikes. Majority of the oblique events have strike between $40° - 50°$ while most normal events have strike between $50° - 70°$ and reverse between $100° - 110°$.
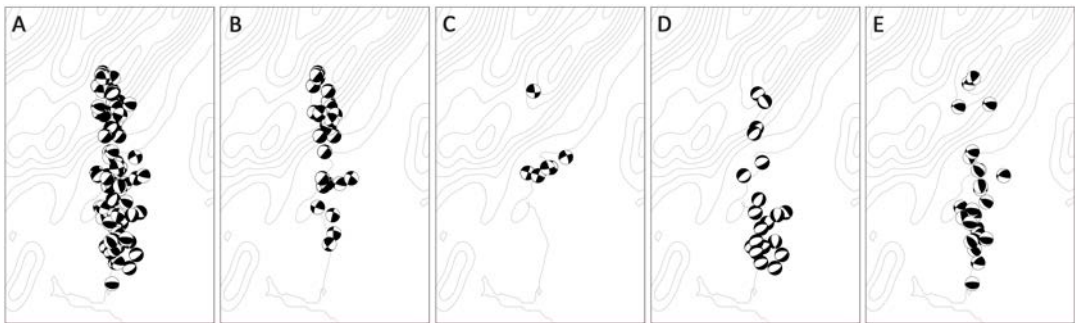
Figure 4.3: Mapped focal mechanisms of events in a swarm in Núphlíð (3a-c in Fig. 4.2). A: All focal mechanism solutions; B: Oblique events; C: Strike-slip events; D: Normal events; E: Reverse events.

5 Stress tensor

5.1 Stress tensor inversion theory

Earthquake focal mechanisms can give valuable information about the local stress field. To calculate stress tensor for events in the Krýsuvík and Fagradalsfjall area we used the stress tensor inversion software STI (Lund and Slunga, 1999). It is based on two fundamental assumptions: The state of stress in the space and time of the earthquake activity is homogeneous, and the maximum shear traction on the fault plane is parallel to the slip direction. The inversion provides four of the six components of the stress tensor: the direction of the principal stresses σ_1, σ_2 and σ_3 and the relative size of the intermediate stress, σ_2, with respect to σ_1 and σ_3, $R = (\sigma_1 - \sigma_2)/(\sigma_1 - \sigma_3)$. Additionally, the direction of the maximum horizontal stress S_H can be computed (Lund and Townend, 2007).

The inversion method works by minimizing the angle α which lies in the fault plane between the shear stress direction τ and the slip direction $\mathbf{s}$, $\alpha = \cos^{-1}(\tau \cdot s)$. The algorithm performs a grid search over a half-space of principal stress directions by fixing the direction of σ_1 and rotating σ_2 and σ_3 in the plane perpendicular to σ_1. For each event a range of possible focal mechanisms is considered. Inherent in all

double-couple focal solutions is an ambiguity between the two possible nodal planes. The software chooses which nodal plane applies either based on which has the lowest misfit for each event or based on which plane is closer to failure according to the Coulomb failure criterion. The misfits from all of the events are then added into a final misfit for the current stress tensor.

5.2 Stress tensor inversion results

Stress tensors inversions were performed seperately on focal mechanisms of events in the Krýsuvík area and in the Fagradalsfjall area. The data in Krýsuvík was furthed divided into 12 subsets, the same as in Chapter 4. The results are presented in Fig. 5.1-5.3 as lower hemisphere projections of the principal stress directions, with the best fit stress tensor represented by filled black symbols (a square for σ_1, diamond for σ_2 and triangle for σ_3). The stress tensor for the Fagradalsfjall events (Fig. 5.1) shows a NW-SE trending σ_3 dipping $\sim 50°$. The maximum horizontal stress, S_H, lies in the NNE-SSW direction (histogram on the periphery). Fig. 5.2 shows the results of the stress tensor inversions for the events in the Krýsuvík area. They show that a majority of the stress states have a stable, close to horizontal σ_3 trending NW-SE. Some exceptions are noted. Subset 1 reveals a reverse stress state while a majority of the stress tensor solutions with a horizontal σ_3 are strike-slip stress states. Subsets 3a-c are all part of the Núphlíð swarm which is the subject of section 4.2. In an effort to recover the relevant stress state the swarm was divided into three groups, south, center and north. In each case none of the principal stress axes lies close to vertical, which contradicts Anderson's theory of faulting (Anderson, 1951). Anderson's theory states that the surface of the Earth acts as a free surface and therefore two of the principal stresses lie parallel to the surface and the third is

perpendicular. The mixed stress condition could be explained by faulting taking place on non-optimally oriented faults. However, σ_3 lies consistently in the NW-SE direction. Subsets 4 and 5 share the same characteristics as 3a-c, with none of the principal axes lying close to vertical and σ_3 dipping $\sim 45°$ from horizontal. In the stress tensor solution for subset 9, σ_3 is horizontal while σ_1 and σ_2 plunge $45°$ from horizontal, indicating an oblique stress state. All of the subsets except 3c show a stable direction of maximum horizontal stress, S_H, pointing in a NNE-SSW to NE-SW direction (histogram on the periphery).
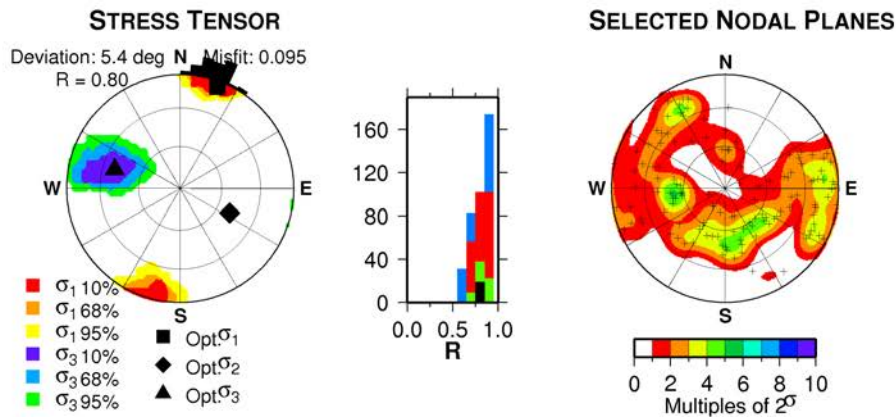
Figure 5.1: Stress tensor results for events in Fagradalsfjall. The left plot shows the principal stress directions on a lower hemisphere projection, with the best fit stress tensor represented by filled black symbols (a square for σ_1, diamond for σ_2 and triangle for σ_3). The confidence regions for σ_1 are shown in warm colors and for σ_3 in cold colors. On the periphery of the plot is a histogram of the 95% confidence level of the maximum horizontal stress, S_H. In addition it shows on the right a plot displaying the poles of the normals of the fault planes selected during the inversion. The crosses indicate the poles and Kamb contours surround them. In between the two plots is a box portraying the best fit R as a black rectangular with blue, red and green histograms as the 95%, 68% and 10% confidence levels, respectively.

Fig. 5.3 shows the stress tensors for the twelve subsets of Krýsuvík as well as histograms of the value of R (box in the center) and plots depicting the poles of the normals of the fault planes selected during the inversion (circles on the right). R is generally high (>0.8) indicating that $\sigma_2 \approx \sigma_3$. Three exceptions are observed. In

subsets 4, 8, and 9 the value is lower suggesting a high value of σ_1 compared to the other principal stress axes. The nodal planes selected during the inversion process largely fall into three catagories: vertical N-S oriented planes, steep NE-SW planes, and E-W oriented planes dipping towards north. Mapping of surface fractures on the Reykjanes Peninsula shows that fractures striking NE-SW are the most abundant while N-S striking strike-slip faults are the longest (Clifton and Kattenhorn, 2006). Hardly any E-W oriented fractures were recorded on the surface. $R = 0.8$ in Fagradalsfjall indicates as well that $\sigma_2 \approx \sigma_3$ (Fig. 5.1). The poles of the normals of the fault planes are diverse indicating four different types of nodal planes: steep and gently dipping N-S oriented planes, as well as steep and gently dipping NE-SW oriented planes. Hjaltadóttir and Vogfjörð (2006a) found in a study of relocated events in Fagradalsfjall that most of the faults in the area had a close to vertical dip with a N-S and NE-SW strike. Despite the variety of focal mechanisms used for the tensor inversions, the results are consistent and share certain characteristics with results from events recorded in 1997-2006 (Keiding et al., 2008). They found a stress field with a stable horizontal σ_3, trending NW-SE. Their average direction of the least compressive horizontal stress, S_h, was calculated as N(120 ± 6)°E. This compares well with our average direction of N(120 ± 10)°E (1σ standard deviation) for S_h and in accordance with their results for the average direction of the greatest horizontal strain rate ($\dot{\epsilon}_{Hmax}$) N(121 ± 3)°E (1σ standard deviation of the circular mean) (Keiding et al., 2008).
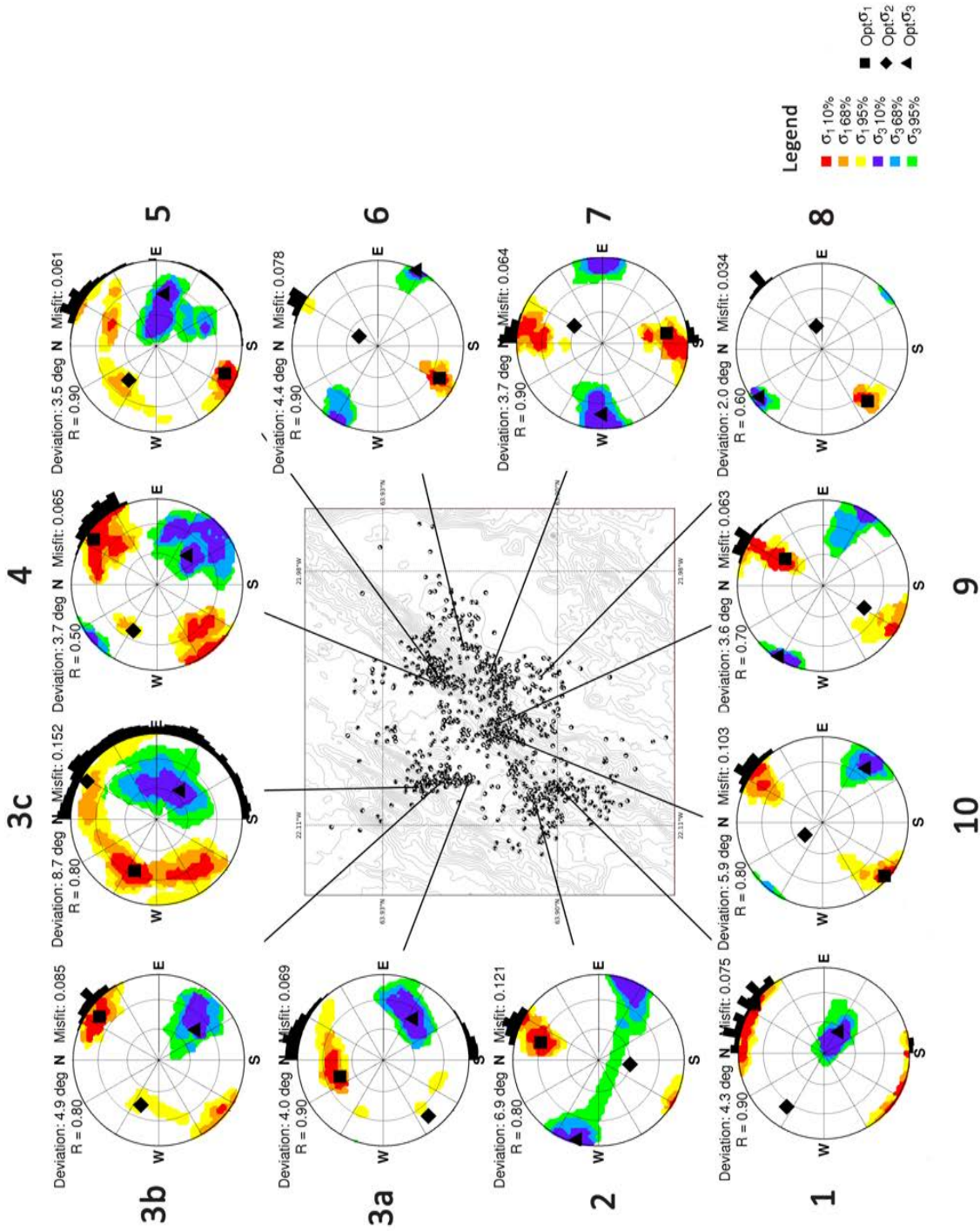
Figure 5.2: Map of the Krýsuvík area showing the locations of events. Surrounding the map are lower hemisphere projections of the stress tensor inversion results for the twelve subsets described in Chapter 4. See explanations in Fig. 5.1.
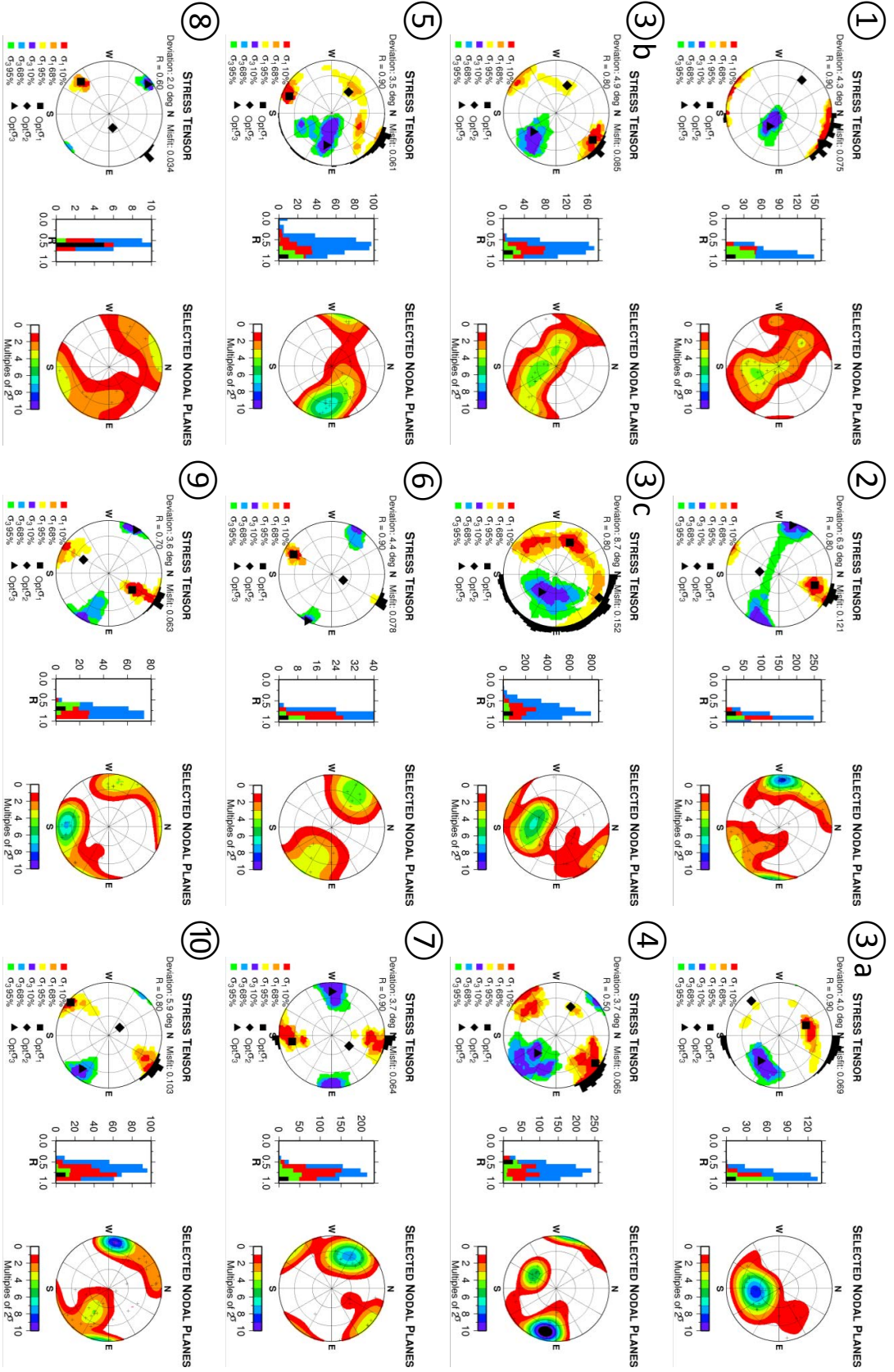
Figure 5.3: Stress tensors for the twelve subsets in the Krýsuvík area. See explanations in Fig. 5.1.

6 Discussion

An updoming in earthquake hypocenters is apparent beneath the Krýsuvík geother-mal system (Fig. 3.2), suggesting a change in the depth to the brittle-ductile bound-ary (Fig. 3.6). This correlates with evidence of a low P-wave anomaly at 5-8 km depth (Franco, 2013) and a low resistivity anomaly at 1.5-5 km depth (Hersir et al., 2013). Very few earthquakes originate within the low P-wave anomaly. However, no S-wave attenuation is detected, suggesting that the anomaly can not be explained by the presence of a large, contigiuous body of magma.

Our results of focal mechanism solutions for 1,063 events in Fagradalsfjall and Krýsu-vík areas show that a wide range of focal mechanisms coexisted in time and space. A further examination of a swarm in northern Núphlíðarháls (Chapter 4.3) showed that events which took place within a period of two days and limited to a NS-trending distribution at a depth of 1-3 km have varied focal mechanism solutions. Hjaltadóttir and Vogfjörð (2006a) found by detailed analysis of relocated events on faults in the Fagradalsfjall area that generally events shared focal mechanism solu-tions of right-lateral strike-slip motion with a normal faulting component or in some cases reverse faulting mechanisms. Some of the determined faults have rake which varies with time (1-5 years), indicating a change in the local stress field. A similar survey of earthquake activity in Þeistareykir and Bjarnaflag in the Northern Vol-

canic Zone revealed a large variation in the rake of mapped faults (Hjaltadóttir and Vogfjörð, 2006b). Unlike the events in our study in Fagradalsfjall and Krýsuvík the activity in Þeistareykir and Bjarnaflag are dispersed over a ~15 year period which could explain the variety in the direction of rake. In another survey, Lippitsch et al. (2005) researched microseismicity in the Torfajökull volcanic system located in the southern highlands of Iceland, on the boundary of the South Iceland Seismic Zone and the Eastern Volcanic Zone. The data was recorded with a temporary network of 20 stations and 9 surrounding permanent stations. They found that fault plane solutions of seismicity in the northwestern part of the caldera correspond to a NW-SE extensional tectonic regime reflected in NE-SW trending faults and fissures in the area. Seismicity within the caldera on the other hand seems to be controlled by a caldera subsidence. Two events were reported to have a thrust faulting mechanism which they interpret as magmatic events. The reverse events recorded in Krýsuvík are not isolated events and give no indication of magmatic involvement. An additional case involves an increase in seismic activity accompanying a period of uplift in 1994-1998 in the Hengill volcanic system in southwest Iceland (see Fig. 2.1). This has been interpreted as being related to an inflation of a magma chamber at depth (Feigl et al., 2000; Hreinsdottir, 1999). Sigmundsson et al. (1997) suggest that the inflation works as an earthquake trigger in an already stressed area.

The FPFIT computer program used to calculate the focal mechanism solutions assumes a double-couple fault plane solutions, only considering pure shear slip in the fault plane and excluding any volume change at the source (Reasenberg and Oppenheimer, 1985). Julian and Foulger (2004) warn that this assumption may not be applicable in geothermal areas. They recommend calculating a complete moment-tensor earthquake mechanism in order to bring out the volumetric component. Foulger et al. (2004) found evidence for non-double-couple microearthquakes

when analysing 26 microearthquakes from the Long Valley caldera in California. The events occured during an active deformation period in the area related to the resurgence of a dome. They conclude that many of the events have positive compensated linear-vector dipole (CLVD) components accompanied by a volume increase. They suggest that the flow of fluid is involved in opening tensile cracks. A moment tensor inversion was not performed on our data at this stage and is not the subject of this paper. Other possible explanations for the occurrence of different faulting events in the same place and time are that events take place on non-optimally oriented faults or are caused by block faulting.

According to the MORVEL plate motion model (DeMets et al., 2010) the spreading rate of the North American and Eurasian plates in southwest Iceland is 18.8 mm/yr toward N100.4°E. Einarsson (1991) reports that the minimum compressive stress on the RP found by inverting focal mechanism solutions is consistently horizontal, oriented in a northwesterly direction. Furthermore, he reports that the maximum stress rotates between the vertical direction, causing normal faulting on NE-striking faults, and the horizontal, northeasterly direction resulting in strike-slip faulting on N- or E-striking faults. Hreinsdóttir et al. (2001) found by inversion of GPS measurements on the RP from 1993-1998 an indication of a deep slip rate of 16.8±0.9 mm/yr transcurrent to the Reykjanes Peninsula seismic zone. They concluded that this was in accordance with the parallel velocity component of the NUVEL-1A model (DeMets et al., 1994). However, little extension was observed across the peninsula. They suggest that this discrepancy can be explained by deformation being dominated by rifting during magmatic activity and by transcurrent motion during intermediate periods. Similarly, Clifton and Kattenhorn (2006) found a difference in faulting mechanism during amagmatic and magmatic periods. They report that strike-slip faulting seems to prevail during amagmatic periods while normal faulting dominates

during magmatic periods. Árnadóttir et al. (2006) determined the surface velocity for the Reykjanes Peninsula from GPS data collected between 1992 and 2004. They found that a model of a locking depth of about 8 km with left-lateral deep slip rate of about 17 mm/yr and about 9 mm/yr of opening for the central and eastern part of the peninsula fit the data. Below the locking depth the the crust slips freely. Keiding et al. (2008) estimate from annual GPS surveys on the RP during 2000-2006 a deep motion of 20^{+4}_{-3} mm/yr in the direction of N(100^{+8}_{-6})°E on the Reykjanes Peninsula, in good agreement with the NUVEL-1A model. They also tested another model which included an opening across a N-E oriented dislocation. Their results indicate that left-lateral shear is satisfied on N-S oriented seismic faults with strike-slip motion and opening mainly takes place in the fissure swarms. They note however, that their models do not completely explain the complicated pattern of deformation on the peninsula. Our results of a stable close to horizontal σ_3 and an average direction of N(120 ± 10)°E for the minimum horizontal stress, S_h, seem to correlate with these findings. Some stress tensors reveal a stress state where none of the principal stress axis is close to horizontal. The stress state could be explained by events taking place on non-optimally oriented faults. No indication of a magmatic intrusion is confirmed.

7 Conclusions

This paper focuses on earthquake activity in the Krýsuvík geothermal system during an active deformation period in 2009. A high level of seismic activity was observed during this period. Over 10,000 events were detected of which 6,100 were manually picked and relocated. The events occur in several swarms and generally delineate N-S trending faults with most earthquakes taking place at a depth between 1.5 and 4 km.

In the Krýsuvík area an updoming in the earthquake hypocenters is evident, possibly signifying a change to the depth of the brittle-ductile boundary. The updoming correlates with signs of geothermal activity on the surface, a low P-wave velocity anomaly at 5-8 km depth and a low resistivity anomaly at 1.5-5 km depth. No earthquake activity is observed within the low P-wave velocity anomaly. Furthermore, no evidence of an S-wave attenuation is observed.

Focal mechanisms were calculated for 1,643 events and the 1,063 best determined solutions were used for further analysis. A wide range of faulting mechanisms characterizes the activity, with normal, strike-slip, and reverse faulting events taking place on the same apparent faults in the same swarms. We suggest this is caused by block faulting or events occurring on non-optimally oriented faults. It is possible

that this could also be explained by a component of volume increase not included in the double-couple fault plane solutions.

Stress tensor inversions were performed on focal mechanism solutions of events in both Krýsuvík and Fagradalsfjall. The data in Krýsuvík was further subdivided into twelve subsets. We conclude that the stress field in the area is characterized by a stable, close to horizontal σ_3 trending in a NW-SE direction. An average value for the least compressive stress, S_h, in the Krýsuvík subsets was found to be N$(120 \pm 10)°$E.

Bibliography

K. Aki and P. G. Richards. *Quantitative seismology.* University Science Books, 2nd edition edition, 2002.

E. M. Anderson. *The Dynamics of Faulting and Dyke Formation with Applications to Britain.* Oliver and Boyd, 1951.

J. Angelier, A. Tarantola, B. Valette, and S. Manoussis. Inversion of field data in fault tectonics to obtain the regional stress - I. Single phase fault populations: a new method of computing the stress tensor. *Geophys. J. Int.*, 69(3):607–621, 1982. doi: 10.1111/j.1365-246X.1982.tb02766.x.

A. E. Clifton and S. A. Kattenhorn. Structural architecture of a highly oblique divergent plate boundary segment. *Tectonophysics*, 419:27–40, 2006. doi: 10.1016/j.tecto.2006.03.016.

J. Decriem, Th. Árnadóttir, A. Hooper, H. Geirsson, F. Sigmundsson, M. Keiding, B. G. Ófeigsson, S. Hreinsdóttir, P. Einarsson, P. LaFemina, and R. A. Bennett. The 2008 May 29 earthquake doublet in SW Iceland. *Geophys. J. Int.*, 181:1128–1146, 2010. doi: 10.1111/j.1365-246X.2010.04565.x.

C. DeMets, R. G. Gordon, and D. F. Argus. Geologically current plate motions. *Geophys. J. Int.*, 181, 2010. doi: 10.1111/j.1365-246X.2009.04491.x.

C. G. DeMets, R. G. Gordon, D. F. Argus, and S. Stein. Effect of recent revisions to the geomagnetic reversal time scale on estimates of current plate motions. *Geophys. Res. Lett.*, 21:2191–2194, 1994.

P. Einarsson. Earthquakes and present-day tectonism in Iceland. *Tectonophysics*, 189:261–279, 1991.

P. Einarsson. Plate boundaries, rifts and transforms in Iceland. *Jökull*, (58):35–58, 2008.

P. Einarsson and S. Björnsson. Jarðskjálftamælingar á raunvísindastofnun háskólans. In Þorsteinn I. Sigfússon, editor, *Í hlutarins eðli: Afmælisrit til heiðurs Þorbirni Sigurgeirssyni prófessor.* Menningarsjóður og Eðlisfræðifélag Íslands, 1987.

P. Erlendsson and P. Einarsson. The Hvalhnúkur Fault, a strike-slip fault mapped within the Reykjanes Peninsula oblique rift, Iceland. In B. Thorkelsson, editor, *Seismology in Europe*, pages 498–504, Reykjavík, 1996.

K. L. Feigl, J. Gasperi, F. Sigmundsson, and A. Rigo. Crustal deformation near Hengill volcano, Iceland 1993-1998: Coupling between magmatic activity and faulting inferred from elastic modeling of satellite radar interferograms. *J. Geophys. Res.*, 105(B11):26,655–25,670, 2000.

G. R. Foulger, B. R. Julian, D .P. Hill, A. M. Pitt, P. E. Malin, and E. Shalev. Non-double-couple microearthquakes at Long Valley caldera, California, provide evidence for hydraulic fracturing. *Journal of Volcanology and Geothermal Research*, 132(1):45–71, 2004.

A. Franco. Personal communication, 2013.

L. Geoffroy and C. Dorbath. Deep downward fluid percolation driven by localized crust dilatation in Iceland. *Geophys. Res. Lett.*, 35(L17302), 2008. doi: 10.1029/ 2008GL034514.

J. W. Gephart and D. W. Forsyth. An improved method for determining the regional stress tensor using earthquake focal mechanism data: Application to the San Fernando earthquake sequence. *J. Geophys. Res.*, 89, 1984.

G. P. Hersir, K. Árnason, and A. M. Vilhjálmsson. 3D inversion of magnetotelluric (MT) resistivity data from Krýsuvík high temperature geothermal area in SW Iceland. In *Proceedings of the thirty-eighth Workshop on Geothermal Reservoir Engineering*, 2013.

S. Hjaltadóttir and K. S. Vogfjörð. Kortlagning sprungna í Fagradalsfjalli á Reykjanesskaga með smáskjálftum. Technical report, Iceland Meteorological Office, 2006a. Skýrsla VÍ-ES-01.

S. Hjaltadóttir and K. S. Vogfjörð. Sprungukortlagning við Þeistareyki og Bjarnaflag með háupplausnarstaðsetningum smáskjálfta. Technical report, Iceland Meteorological Office, 2006b. Skýrsla VÍ 2011/016.

S. Hreinsdottir. GPS geodetic measurements on the Reykjanes Peninsula, SW Iceland: Crustal deformation from 1993-1998. Master's thesis, University of Iceland, 1999.

S. Hreinsdóttir and K. Michalczewska. Krísuvík - GPS time series. `strokkur.raunvis.hi.is/~sigrun/KRIV.html`. Viewed March 5, 2013.

S. Hreinsdóttir, P. Einarsson, and F. Sigmundsson. Crustal deformation at the oblique spreading Reykjanes Peninsula, SW Iceland: GPS measurements from 1993 to 1998. *J. Geophys. Res.*, 106(B7):13803–13816, 2001.

48

S. Hreinsdóttir, Th. Árnadóttir, J. Decriem, H. Geirsson, A. Tryggvason, R. A. Bennett, and P. LaFemina. A complex earthquake sequence captured by the continuous GPS network in SW Iceland. *Geophys. Res. Lett.*, 36(L12309), 2009. doi: 10.1029/2009GL038391.

S. Husen and J. L. Hardebeck. Earthquake location accuracy. *Community Online Resource for Statistical Seismicity Analysis*, 2010. doi: 10.5078/corssa-55815573.

J .C. Jaeger, N. G. W. Cook, and R. W. Zimmerman. *Fundamentals of Rock Mechanics*. Blackwell, 4th edition, 2007.

S. P. Jakobsson, J. Jónsson, and F. Shido. Petrology of the Western Rreykjanes Peninsula, Iceland. *Journal of Petrology*, 19:669–705, 1978.

B. R. Julian and G. R. Foulger. Microearthquakes focal mechanisms. *GRC Bulletin*, pages 166–171, July/August 2004.

M. Keiding, Th. Árnadóttir, E. Sturkell, H. Geirsson, and B. Lund. Strain accumulation along an oblique plate boundary: The Reykjanes Peninsula, southwest Iceland. *Geophys. J. Int.*, 172:861–872, 2008. doi: 10.1111/j.1365-246X.2007.03655.x.

M. Keiding, B. Lund, and Th. Árnadóttir. Earthquakes, stress, and strain along an obliquely divergent plate boundary: Reykjanes Peninsula, southwest Iceland. *J. Geophys. Res.*, 114, 2009. doi: 10.1029/2008JB006253.

P. C. LaFemina, T. H. Dixon, R. Malservisi, Th. Árnadóttir, E. Sturkell, F. Sigmundsson, and P. Einarsson. Geodetic GPS measurements in south Iceland: Strain accumulation and partitioning in a propagating ridge system. *J. Geophys. Res.*, 110(B11405), 2005.

T. Lay and T. C. Wallace. *Modern Global Seismology*. Academic Press, 1995.

R. Lippitsch, R. S. White, and H. Soosalu. Precise hypocenter relocation of microearthquakes in a high-temperature geothermal field: The Torfajökull central volcano, Iceland. *Geophys. J. Int.*, 160:370–387, 2005. doi: 10.1111/j.1365-246X. 2005.02467.x.

B. Lund. Visualizing the stress tensor: Stress ellipse and Mohr circle. `www.geofys. uu.se/bl/Avh/node11.html`, 2000. Viewed on April 22nd, 2013.

B. Lund. Ternary plot software. Personal communication, 2012. Uppsala University.

B. Lund and R. Slunga. Stress tensor inversion using detailed microearthquake information and stability constraints: Application to Ölfus in southwest Iceland. *J. Geophys. Res.*, 104(B7):14947–14964, 1999.

B. Lund and J. Townend. Calculating horizontal stress orientations with full or partial knowledge of the tectonic stress tensor. *Geophys. J. Int.*, 170, 2007.

A. J. Michael. Determination of stress from slip data: Faults and folds. *J. Geophys. Res.*, 89(B13):11517–11526, 1984.

K. Michalczewska, S. Hreinsdóttir, Th. Árnadóttir, S. Hjaltadóttir, Th. Ágústsdóttir, M. T. Guðmundsson, H. Geirsson, F. Sigmundsson, and G. Guðmundsson. Inflation and deflation episodes in the Krisuvik volcanic system. In *AGU fall meeting, San Francicso, USA*, 2012.

C. Pagli, R. Pedersen, F. Sigmundsson, and K. L. Feigl. Triggered fault slip on June 17, 2000 on the Reykjanes Peninsula, SW-Iceland captured by radar interferometry. *Geophys. Res. Lett.*, 30(6):1273, 2003. doi: 10.1029/2002GL015310.

P. A. Reasenberg and D. Oppenheimer. FPFIT, FPPLOT and FPPAGE: Fortran computer programs for calculating and displaying earthquake fault-plane solutions. 1985.

K. Saemundsson. Fissure swarms and central volcanoes of the neovolcanic zones of Iceland. *Geological Journal, special issue*, 10:415–432, 1978.

F. Sigmundsson, P. Einarsson, S. Th. Rögnvaldsson, G. R. Foulger, K. M. Hodgkinson, and G. Thorbergsson. The 1994-1995 seismicity and deformation at the Hengill triple junction, Iceland: Triggering of earthquakes by minor magma injection in a zone of horizontal shear stress. *J. Geophys. Res.*, 102(B7):15151–15161, 1997.

E. Tryggvason. Seismicity, earthquake swarms, and plate boundaries in the Iceland region. *Bulletin of the Seismological Society of America*, 63(4):1327–1348, 1973.

United States Geological Survey. Earthquake glossary. `http://earthquake.usgs.gov/learn/glossary/?term=momenttensor`. Viewed May 16, 2013.

F. Waldhauser. HypoDD: A computer program to compute double-difference hypocenter locations. *U.S. Geol. Surv. Open File Rept. 01-113*, 2001.

F. Waldhauser and W. L. Ellsworth. A double-difference earthquake location algorithm: Method and application to the Northern Hayward Fault, California. *Bulletin of the Seismologial Society of America*, 90(6):1353–1368, 2000.

H. Zhang and C. H. Thurber. Double-difference tomography: The method and its application to the Hayward fault, California. *Bulletin of the Seismological Society of America*, 93(5):1875–1889, 2003. doi: 10.1785/0120020190.

Th. Árnadóttir, H. Geirsson, and P. Einarsson. Coseismic stress changes and crustal deformation on the Reykjanes Peninsula due to triggered earthquakes on 17 June 2000. *J. Geophys. Res.*, 109(B09307), 2004. doi: 10.1029/2004JB003130.

Th. Árnadóttir, W. Jiang, K. L. Feigl, H. Geirsson, and E. Sturkell. Kinematic models of plate boundary deformation in southwest Iceland derived from GPS observations. *J. Geophys. Res.*, 111(B07402), 2006. doi: 10.1029/2005JB003907.